Supplementary Information

Probing the emission dynamics in nitrogen doped carbon dots by reversible capping with mercury (II) through surface chemistry

Dipayan Roy[†], Antika Das[†], Rajarshi Roy[§], Dimitra Das[†], Bikram Kumar Das[‡], Uttam Kumar Ghorai[$], Kalyan Kumar Chattopadhyay[†,‡,*] and Sourav Sarkar[†,*]

[†]School of Materials Science and Nanotechnology, Jadavpur University, Kolkata-700032, India

[‡]Department of Physics, Jadavpur University, Kolkata-700032, India

[§] J. Heyrovsky Institute of Physical Chemistry, Czech Academy of Sciences, Dolejškova 2155/3, 18200 Prague, Czech Republic

[$] Department of Industrial & Applied Chemistry, Swami Vivekananda Research Centre, Ramkrishna Mission Vidyamandir, Belur Math, Howrah 711202, India

*Corresponding author: souravsarkars@gmail.com
                                kalyan_chattopadhyay@yahoo.com

concentration of Hg^{2+}

Section S1: Discussion on UV-vis Absorbance and Band gap

Figure S1 suggests UV-Vis absorption spectroscopy of N-CQD, where three different sets of samples have been prepared at pH~1-2, pH~7, and pH~12. It is observed that the position of n-π^* (~320 nm) at pH~1-2 and pH~12 of 3A and 3B is almost similar in nature with respect to pH~7 (Figure S1a-c).[1] No significant broad absorption maxima are noticed at 350 nm and 250 nm, which are the characteristic features of fluorophores.[2] To evaluate further details, band gap has been calculated from absorption spectra. Figure S1d-f shows Tauc plot of all N-CQDs where two linear parts of the spectra are observed. After extrapolating to x-axis, the band gap is calculated for 3A,3B and 3C to a value of 3.3-3.45 eV,3.8-4.1 eV and 3.5-4.1eV respectively (Figure S1d-f).
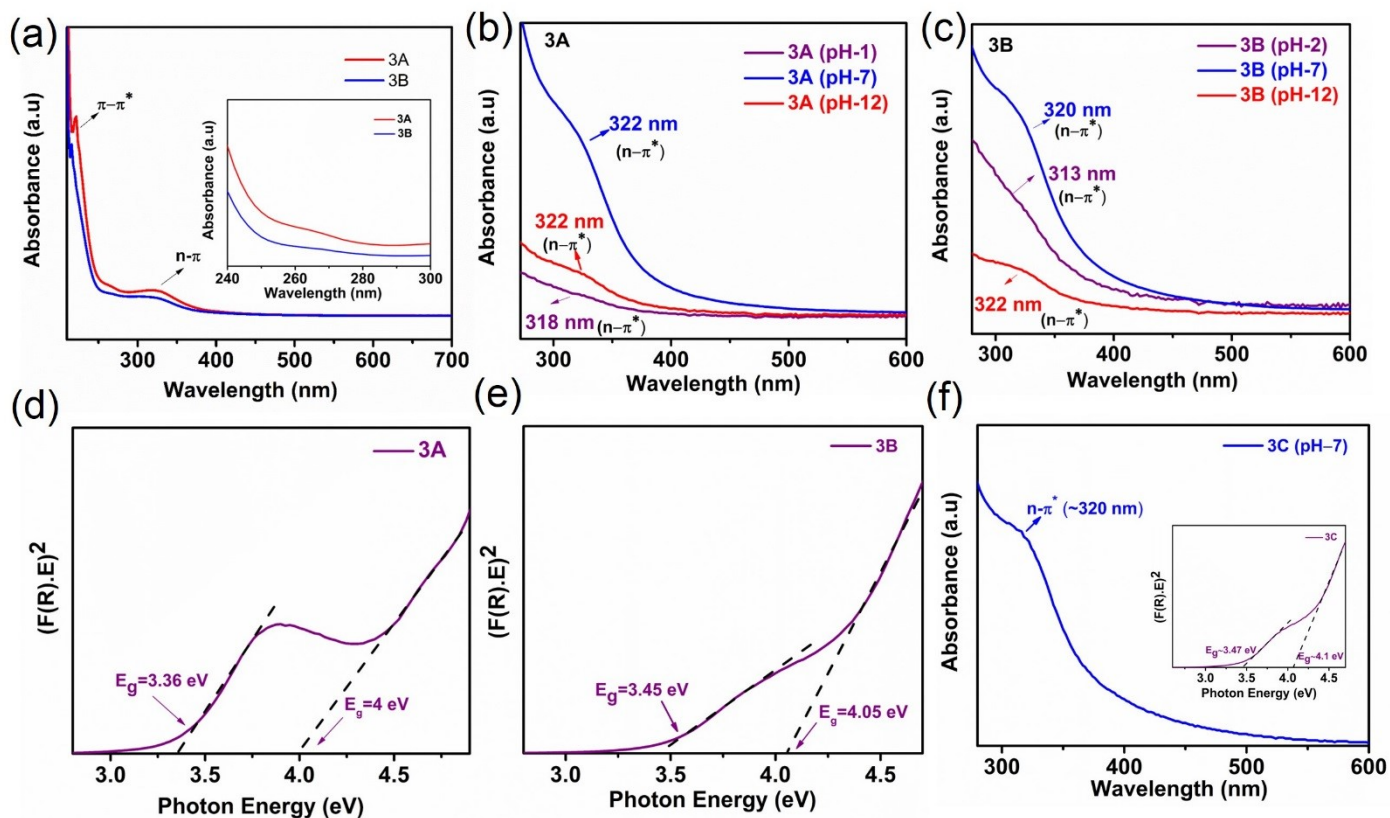

Figure S1: UV-Vis absorption spectroscopy of (a,b) 3A and (a,c) 3B. (d,e) Tauc plot of 3A and 3B. (f) UV-Vis absorbance of 3C (Inset shows Tauc plot of 3C).
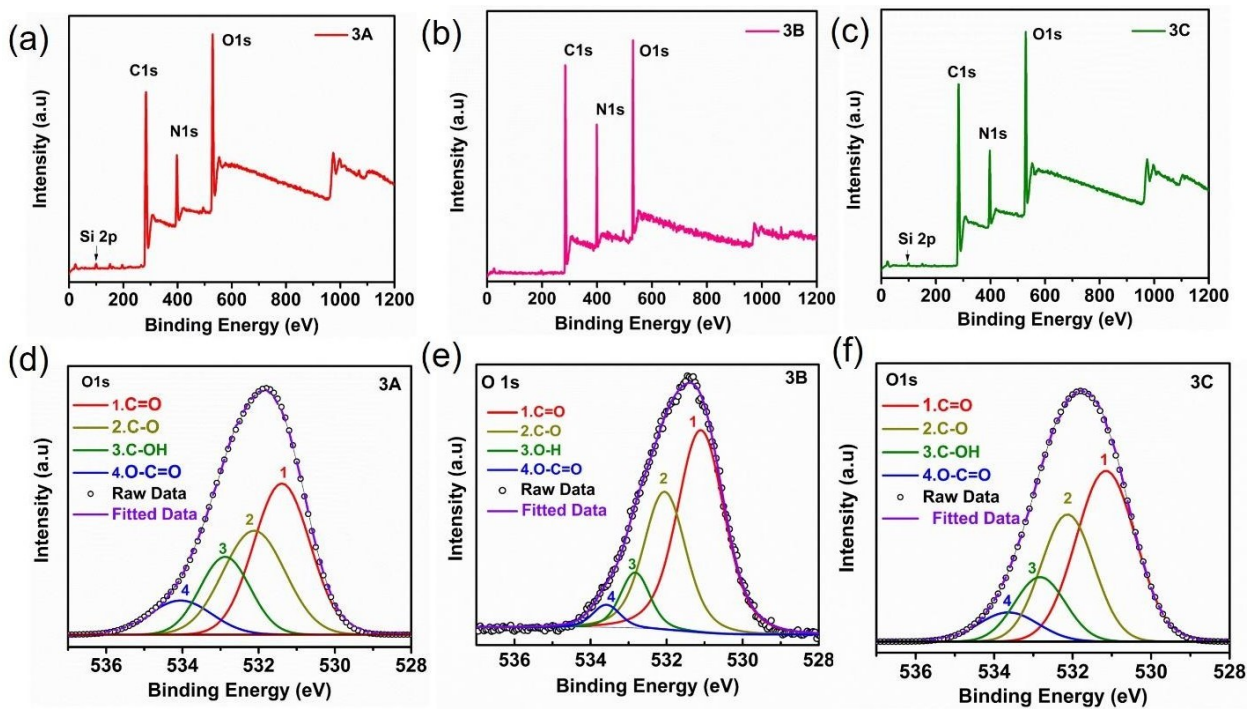
Figure S2: XPS survey spectra of (a) 3A (b) 3B and (c) 3C. High resolution XPS O1s spectra of (d) 3A (e) 3B and (f) 3C.

Section S2: Atomic percentage and functional groups analyses from XPS and FTIR Spectra:

Figure. S3 implies the atomic percentage of functional groups obtained from C1s, N1s, and O1s spectra. It should be noted the increase in reaction time promotes more oxygenation of basal plane of 3C, leading to decrease in sp^2 carbon (C=C) content. The -OH percentage gradually increases from 3A (9.4%) to 3C (12%), shown in Figure S3a. The chemical environment of functional groups is correlated with FTIR spectra shown in Figure S3d. A broad peak around 3450 cm^{-1} and 3200 cm^{-1} attributes to -OH and -NH stretching frequency, respectively, of N-CQD. Similarly, a low intense peak at 2900 cm^{-1} and 1620 cm^{-1} implies -C-H and C=C stretching vibrations, respectively.[3] Interestingly, a small peak around ~1300 cm^{-1} and 1580 cm^{-1} is mainly due to C-N and N-H bending vibration modes.[4] The presence of N-H and C-N mode elucidates the nitrogen atom on the surface of N-CQD. Additionally, the occurrence of three distinct peaks at 1720 cm^{-1}, 1100 cm^{-1}, and 1420 cm^{-1} is mainly due to carbonyl (C=O), epoxy (C-O), and symmetric O-C-O (-COOH) vibrations, respectively.[5]
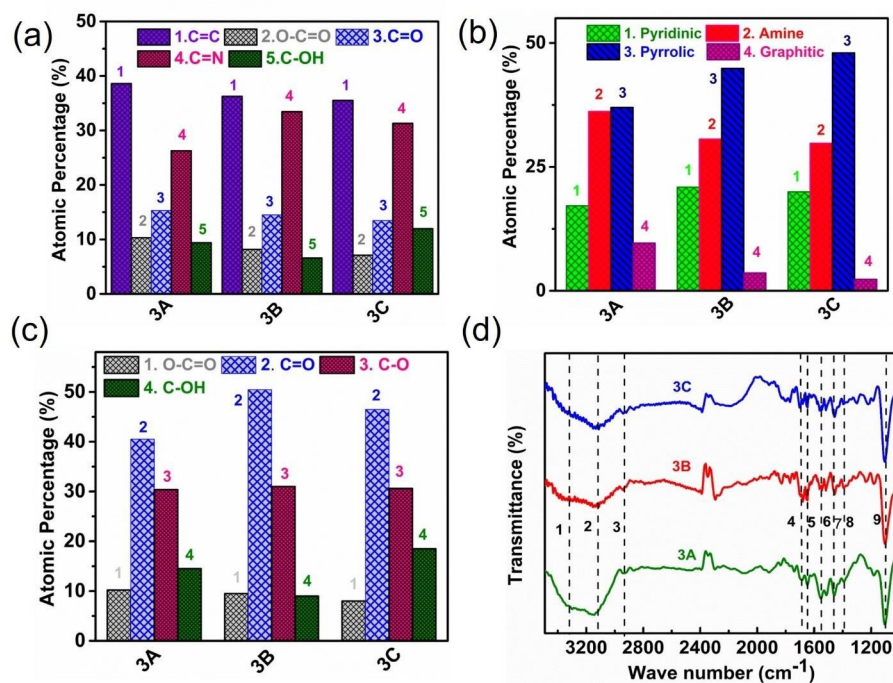

Figure S3: Atomic percentage of different functional groups form (a) C1s, (b) N1s, and (c) O1s spectra of N-CQD (3A,3B,3C). (d)FTIR spectra of 3A,3B, and 3C. (Here, 1-9 denotes different functional groups 1)-N-H stretching, 2) O-H stretching, 3) C-H stretching, 4) C=O, 5) C=C, 6) C-N, 7) N-H bending, 8) O-C=O, 9) C-O stretching frequency.
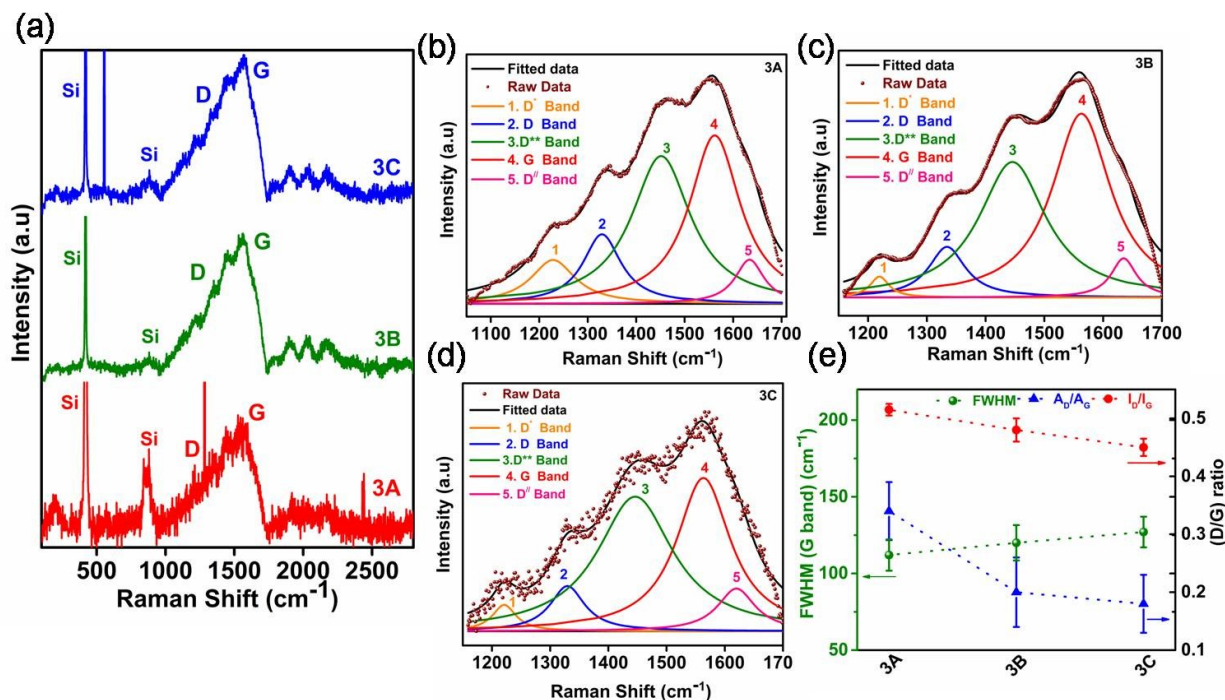
Figure S4: (a) Full range Raman spectra for 3A,3B, and 3C. Deconvoluted Raman spectra consist of first order components for (b) 3A, (c) 3B, and (c) 3C. Brown lines are the original line shape as obtained from spectrometer, and the rest of the colors represent the contributions of different bands. (e) Variation of I_D/I_G, A_D/A_G ratio with FWHM of G band of all N-CQDs.

Section S3: Analyses of PLE at different pH and Concentration:

As lowering the concentration of 3A from 10 mg/ml to 1.65 mg/ml, the intensity of n-π^* absorptions around ~370 nm to 420 nm decreases, most likely due to reduction in H-bonding in polar protic solvent (Figure S5a-b).[6] However, a significant lowering of intensity of the n-π^* absorptions are observed at lower pH~1 (Figure S5d). The protonation of such functional groups hinders the electron transfer towards carbon plane.

Thus, effect lowers the PL and PLE intensity by forming nonradiative groups.[7,8] Figure S6f suggests the blue shift of n-π^* absorption occurs at lower pH (pH~1) due to the formation of nonradiative groups in a highly acidic environment. In highly basic conditions (pH~12), the formation of carboxylate ion and pπ– pπ overlap between NH[-] and aromatic sp[2] ring leads to blue shift of n_{O2p}-π^* and n_{N2p}-π^* transitions.[6,7,9]
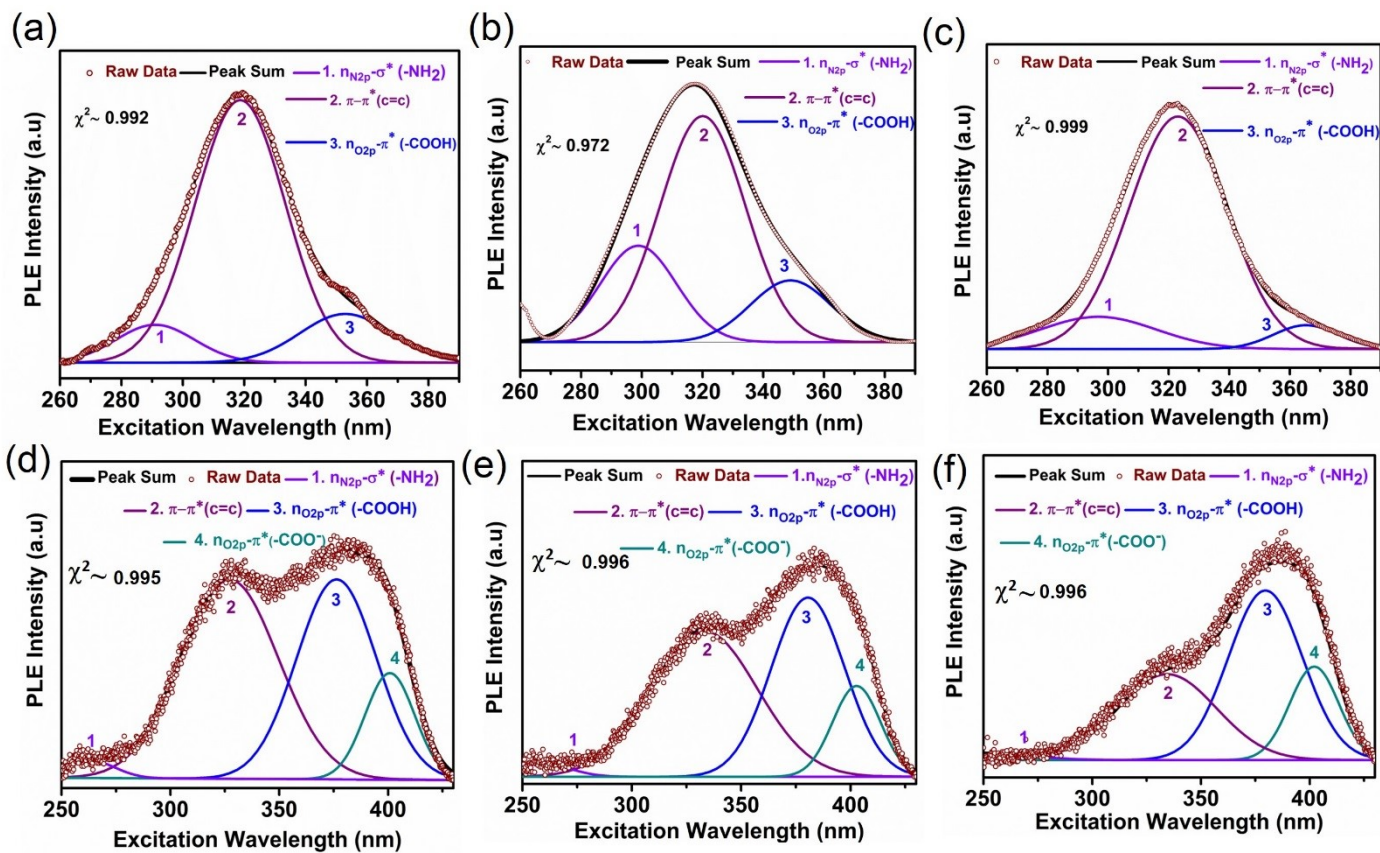
Figure S5: Deconvoluted Photoluminescence excitation (PLE) spectra of (a,d) 3A (b,e,) 3B and (c,f,) 3C at a concentration (6.25 mg/ml) for emission at 410 nm and 445 nm respectively.
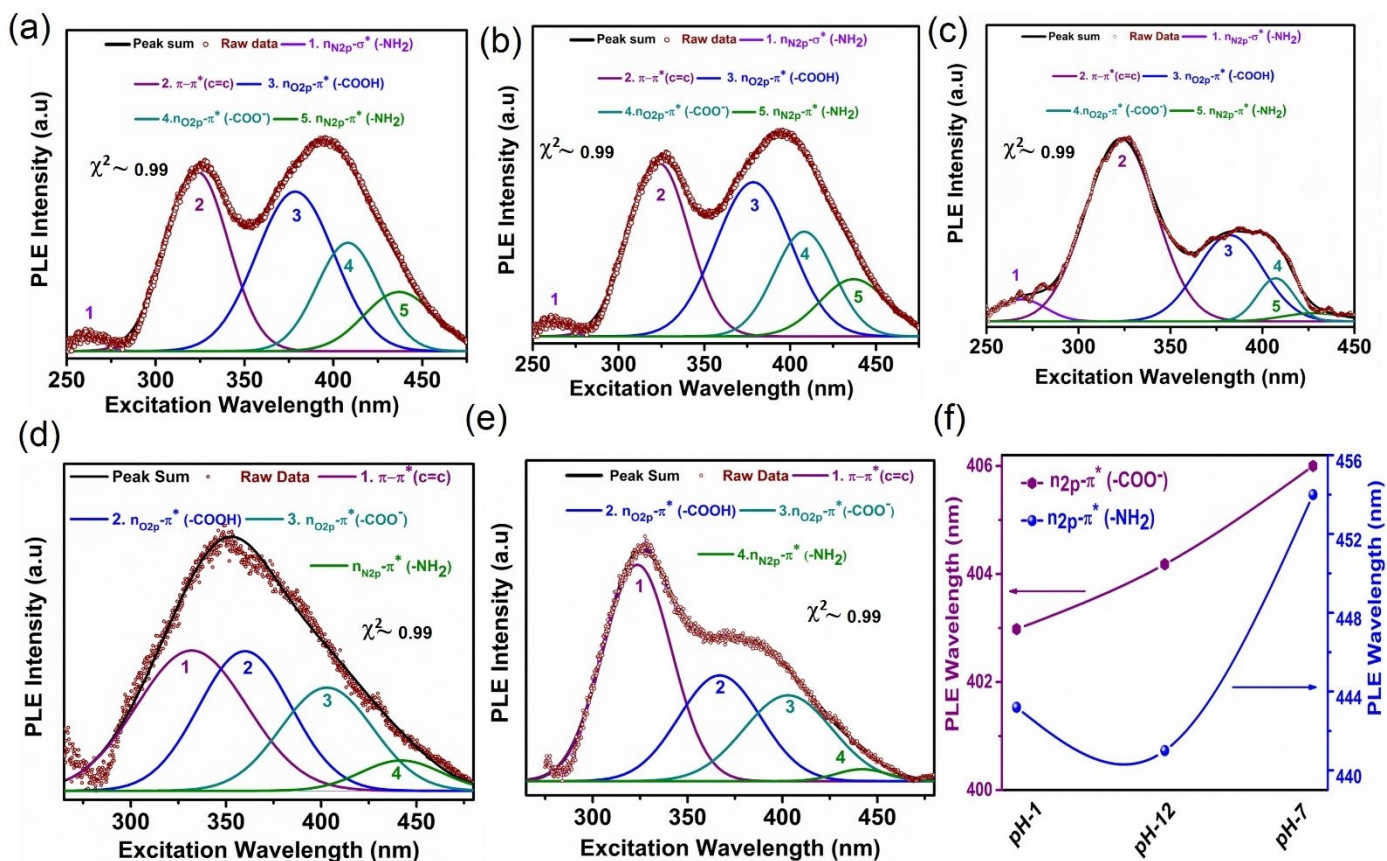
Figure S6: Deconvoluted Photoluminescence excitation (PLE) spectra of 3A for the emission at ~506 nm at concentrations (a) 10 mg/ml and (b) 6.25 mg/ml and (c) 1.65 mg/ml. PLE spectra of 3A at (d) pH~1 and (e) pH~12 at ~506 nm emission wavelength. (f) Position of PLE peak maxima of different n-π^* transitions of 3A at different pH values.
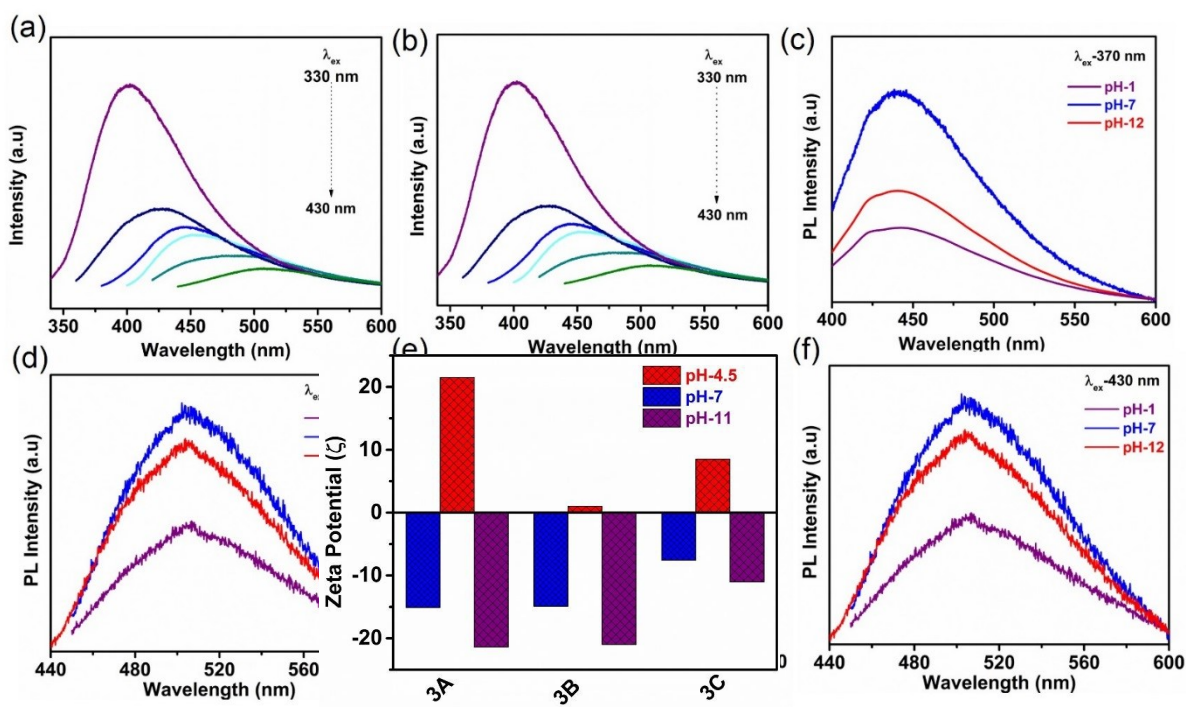
Figure S7: Photoluminescence (PL) spectra of (a) 3B (b) 3C at different excitation wavelengths. Effect of pH on PL spectra of (c,d) 3A and (e,f) 3B at 370 nm and 430 nm excitation wavelength.

Figure S8: Variation of zeta potential (ζ) of N-CQD (3A,3B, and 3C) at different pH values.

At higher pH (pH~10), the ζ becomes negative to -21.4 mV, -20.9 mV, and -10.9 mV for 3A, 3B & 3C, respectively, leading to deprotonation of functional groups, which can boost the electron transfer towards graphitic core in comparison with N-CQD at pH~7 (Figure S8). At which, pH~4.5, ζ of 3A,3B, & 3C become positive to +21.5 mV, +1 mV, and +8.60 mV, respectively, which implies deficiency of electrons at the surface via protonation.

Section S4: Study of PL signals (Peak area, Intensity) of N-CQD with different metal ions

Figure. S9-S12 suggests the maximum relative percentage of area and intensity of peak 1 (π-π^*) shrinks to a value of 13% and 20% (w.r.t 100%), respectively, for 3A under 50 μM Hg^{2+} concentration. In comparison with peak 1 (π-π^*), the percentage of area and intensity of peak 2 (n-π^*) changes to 8.4% and 15.16 % (w.r.t 100%) respectively. Moreover, percentage of area and intensity of peak 1 n_{O2p}-π^* (-COOH) and peak 2 n_{O2p}-π^*/ n_{N2p}-π^* (COO$^-$, NH_2 or amide) modifies to a value of 14%, 25% and 5% and 18% (w.r.t 100%) respectively after incorporating Hg^{2+} ions (Figure S12c&d).
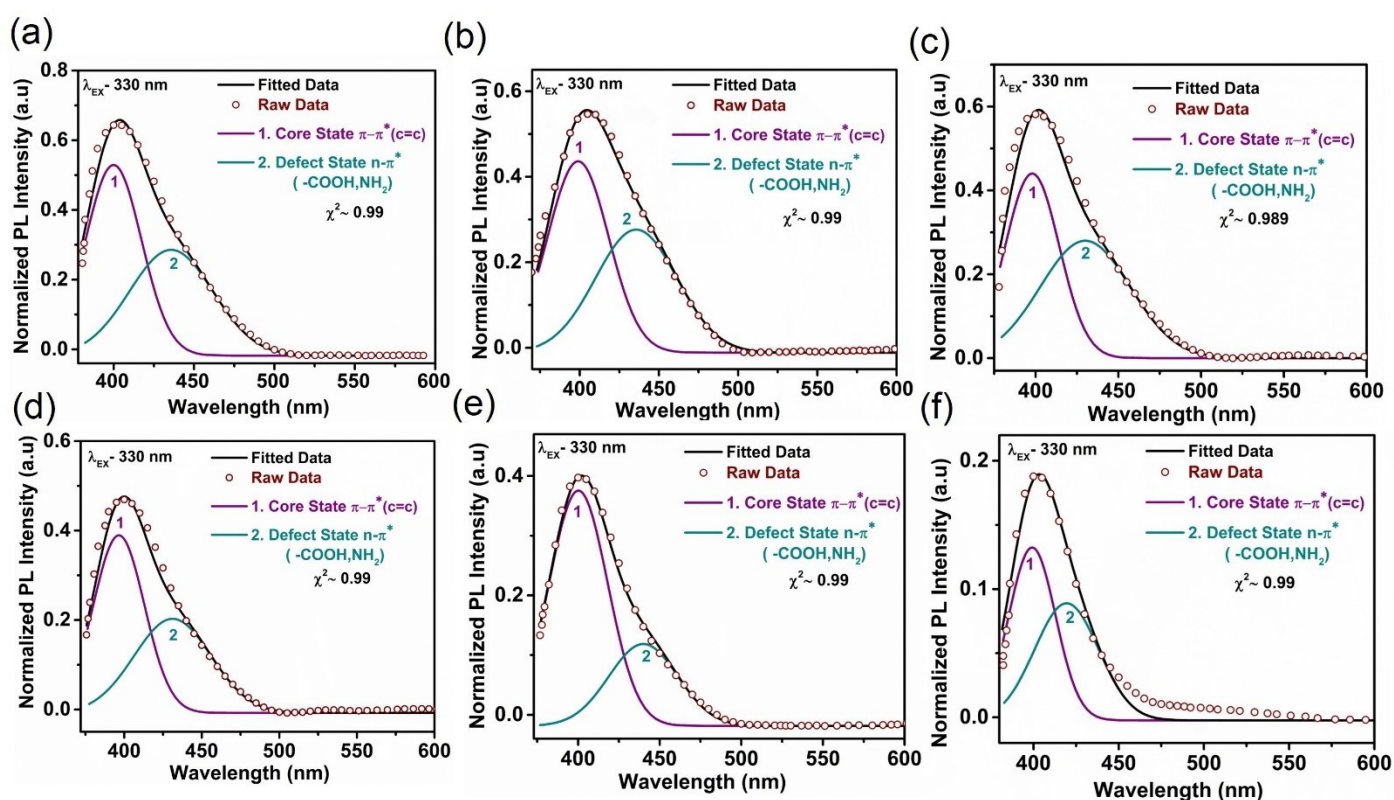
Figure S9: Deconvoluted PL profile of 3A with (a) Zn^{2+} (b) Ni^{2+} (c) Co^{2+} (d) Ag^+ (e) Cu^{2+} and (f) Hg^{2+} at 330 nm excitation.
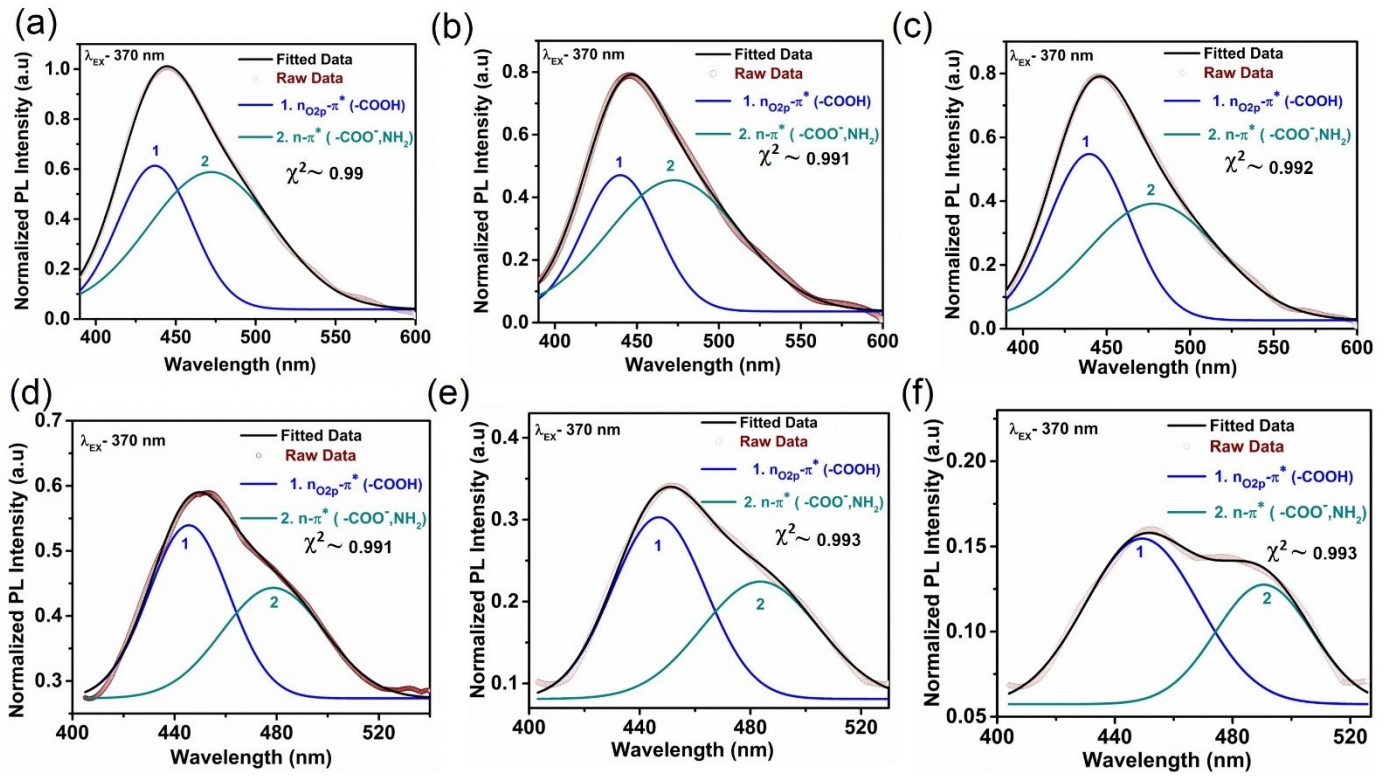
Figure S10: Deconvoluted PL profile of 3A with (a) Zn^{2+} (b) Ni^{2+} (c) Co^{2+} (d) Ag^+ (e) Cu^{2+} and (f) Hg^{2+} at 370 nm excitation.
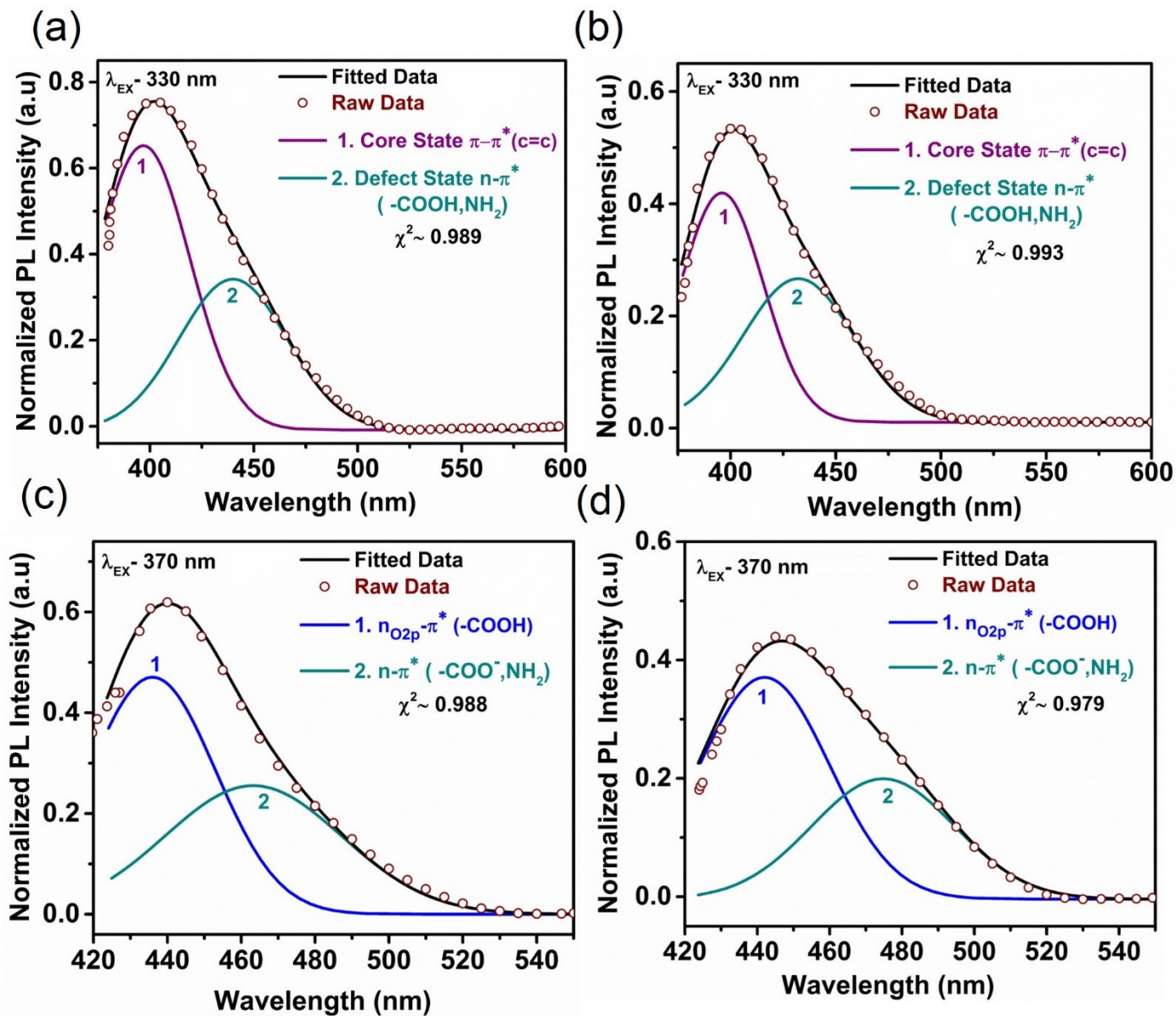
Figure S11: Deconvoluted PL profile of 3A with (a,c) cd^{2+} (b,d) Pb^{2+} at 330 nm and 370 nm excitation.
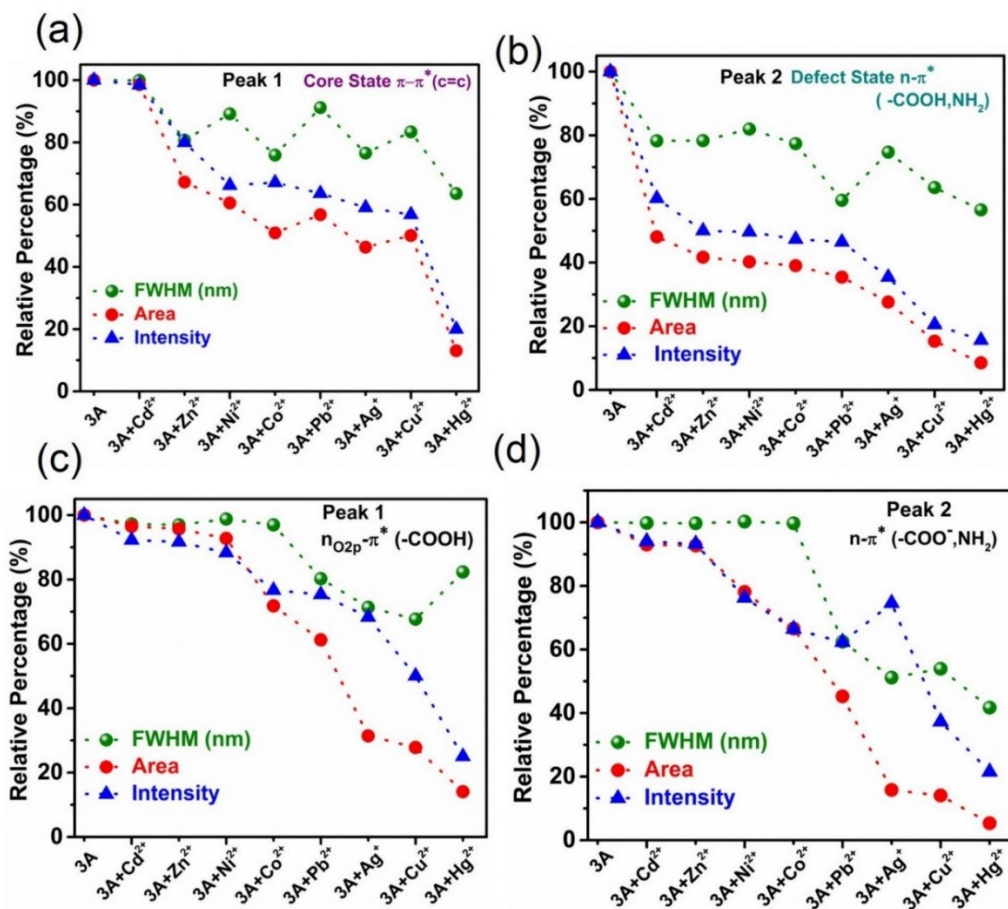
Figure S12: Relative percentage of PL fwhm (nm), area and intensity of (a) peak 1 (π-π^*) (b) peak 2 (n-π^*) (c) peak 1 (n_{O2P}-π^* -COOH) and (d) peak 2 (n_{O2P}-π^* -COO$^-$, NH$_2$) of 3A after adding metal ions (Cd^{2+}, Zn^{2+}, Ni^{2+}, Co^{2+}, Pb^{2+}, Ag$^+$, Cu^{2+}, Hg^{2+}) (Concentrations ~50 µM).
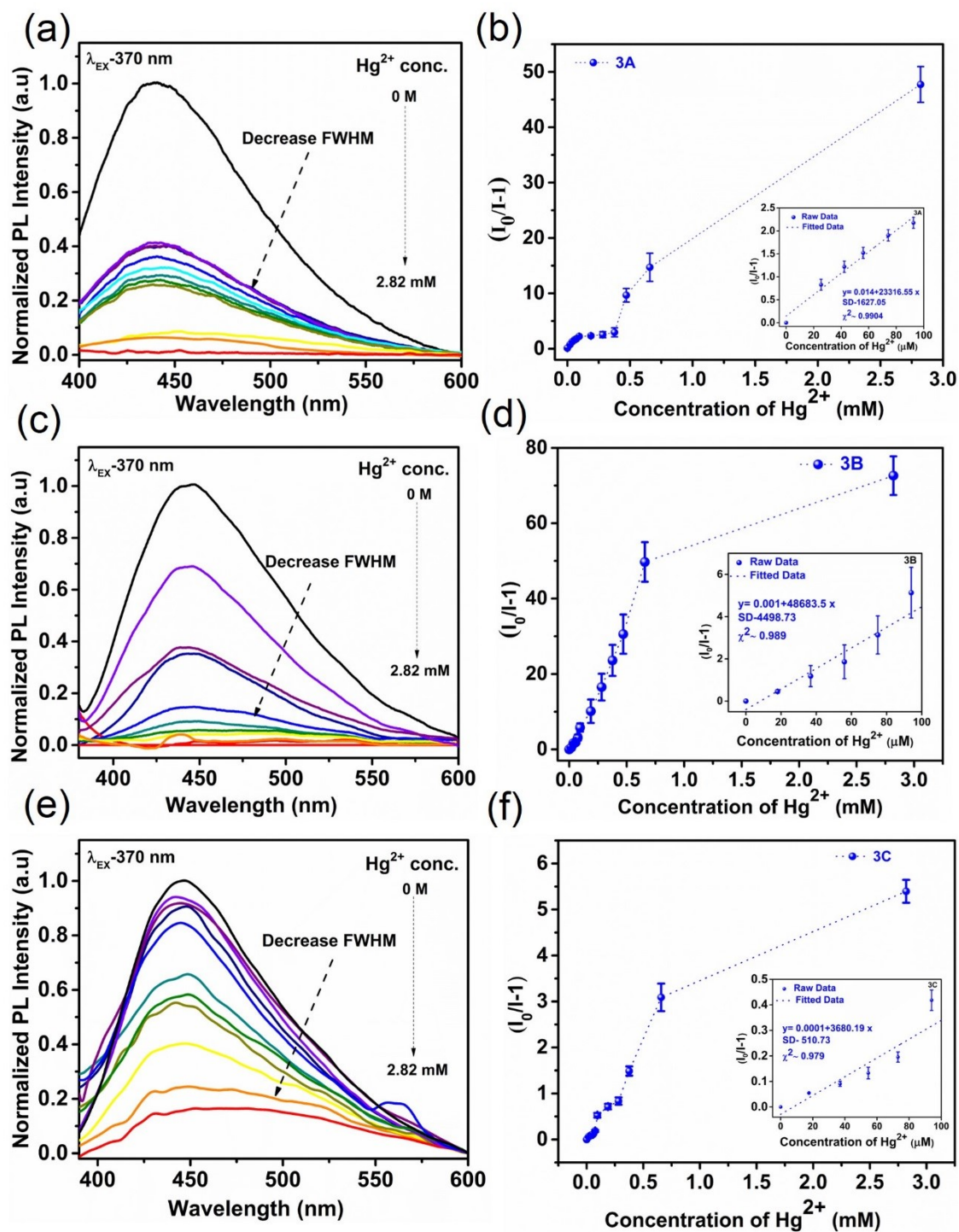
Figure S13: PL quenching of (a) 3a (C) 3B and (e) 3C under different Hg^{2+} concentration (0-2.82 mM). Stern-Volmer plots $(I_0/I)-1$ vs concentration of Hg^{2+} of (b) 3A (d) 3B and (f) 3C (Inset showing linear relationship between $(I_0/I)-1$ vs concentration of Hg^{2+}) at 370 nm excitation.

Section S5: Analyses of PL signals (Peak area, Intensity) of N-CQD with concentration of Hg^{2+} at 330 nm excitation:

Figure S14 implies the emission profile of N-CQD at different Hg^{2+} concentrations ranging from 56 μM to 658 μM. At 56 μM Hg^{2+} the peak area and intensity of 3A, 3B and 3C of peak 1 (π-π*) has diminished to ~18.65%, ~33.2 %, ~51.58 %, ~43.16% and ~99.94%, ~92.59% respectively. The result is congruence with peak 2 (n-π*) to quench the peak area and intensity for 3A, 3B and 3C to ~23.4%, ~42.54 %, ~42.90%, ~48.52% and ~99.9%, ~89% respectively. Similarly, the relative percentage of peak area and intensity of peak 1 change to 18%, 27.2% (3A), 37%, 33% (3B) and 30%, 24% (3C) respectively at 94 μM Hg^{2+} respectively. The peak area and intensity of peak 2 (n-π*) follows the same trend ~26%, ~39% (3A), ~41%, ~42% (3B) and ~26%, ~21% (3C) respectively. Generally, the quenching efficiency follows the trend 3A > 3B > 3C at different Hg^{2+} concentrations.
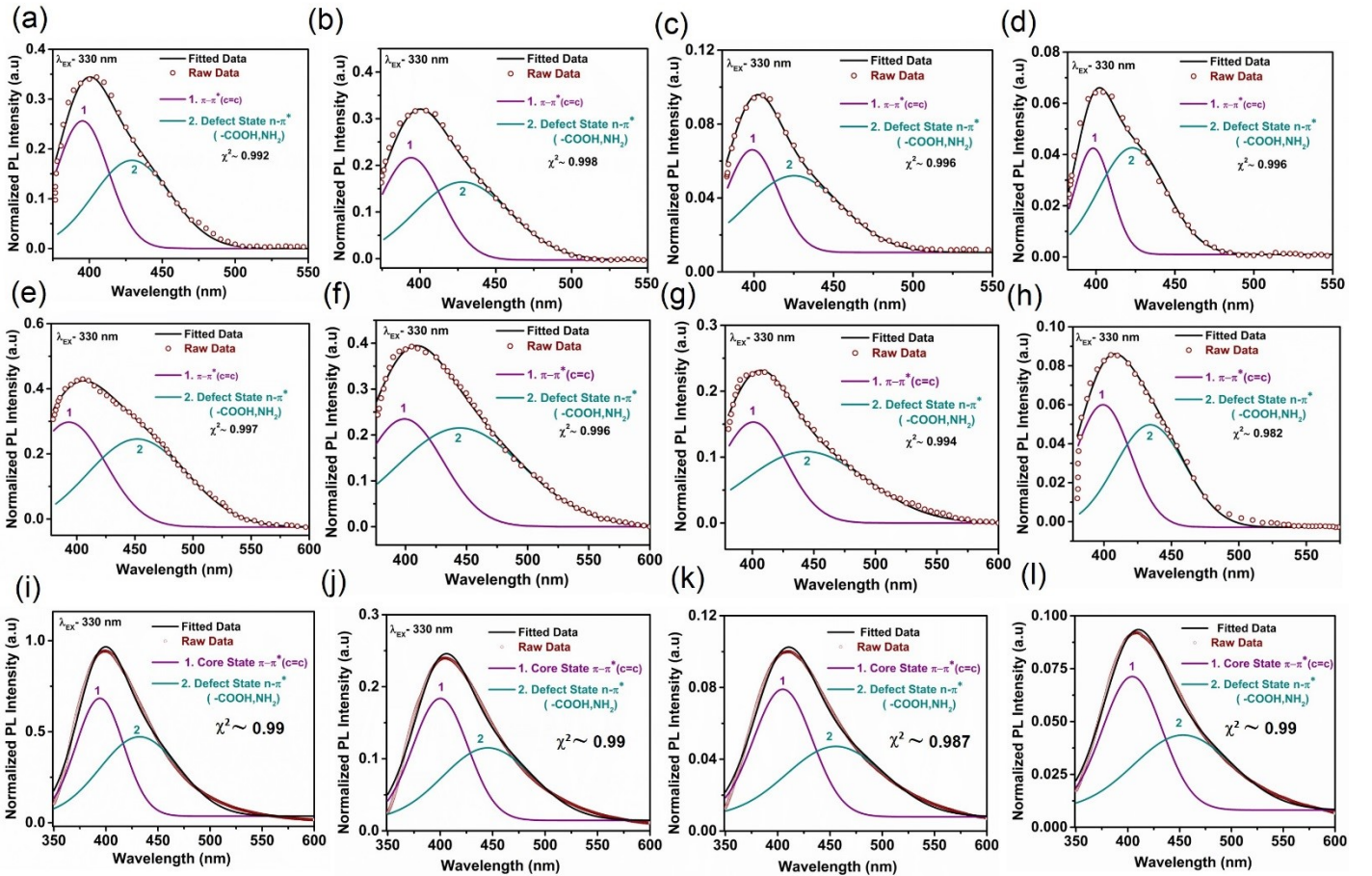
Figure S14: Deconvoluted PL profile of 3A, 3B and 3C with (a,e,i) 56 μM (b,f,j) 94 μM (c,g,k) 376 μM and (d,h,l) 658 μM Hg^{2+} respectively at excitation wavelength 330 nm.

Section S6: Analyses of PL signals (Peak area, Intensity) of N-CQD with concentration of Hg^{2+} at 370 nm excitation:

At 56 µM Hg^{2+} the peak area and intensity of peak 1 n_{O2p}-π^* (-COOH) has diminished to 37%, 36% (3A), 33%, 36% (3B) and 85%, 90% (3C) respectively (Figure S15). In contrast, the peak area and intensity of peak 2 shrinks to 46%, 44% (3A), 33%, 36% (3B) and 93%, 98% (3C) respectively. Strikingly, the change in relative percentage of PL signals of peak area and intensity follows the same trend at 94 µM Hg^{2+} (for 3A~ (peak 1) 35%, 36% and (peak 2) 44%, 42%), (for 3B (peak 1) ~ 10%, 16% and (peak 2) ~ 13%, 18%) and (for 3C (peak 1) ~ 43%, 60% and (peak 2) ~ 57%, 62%). Nevertheless, the quenching efficiency has been calculated follows the order 3B > 3A > 3C.
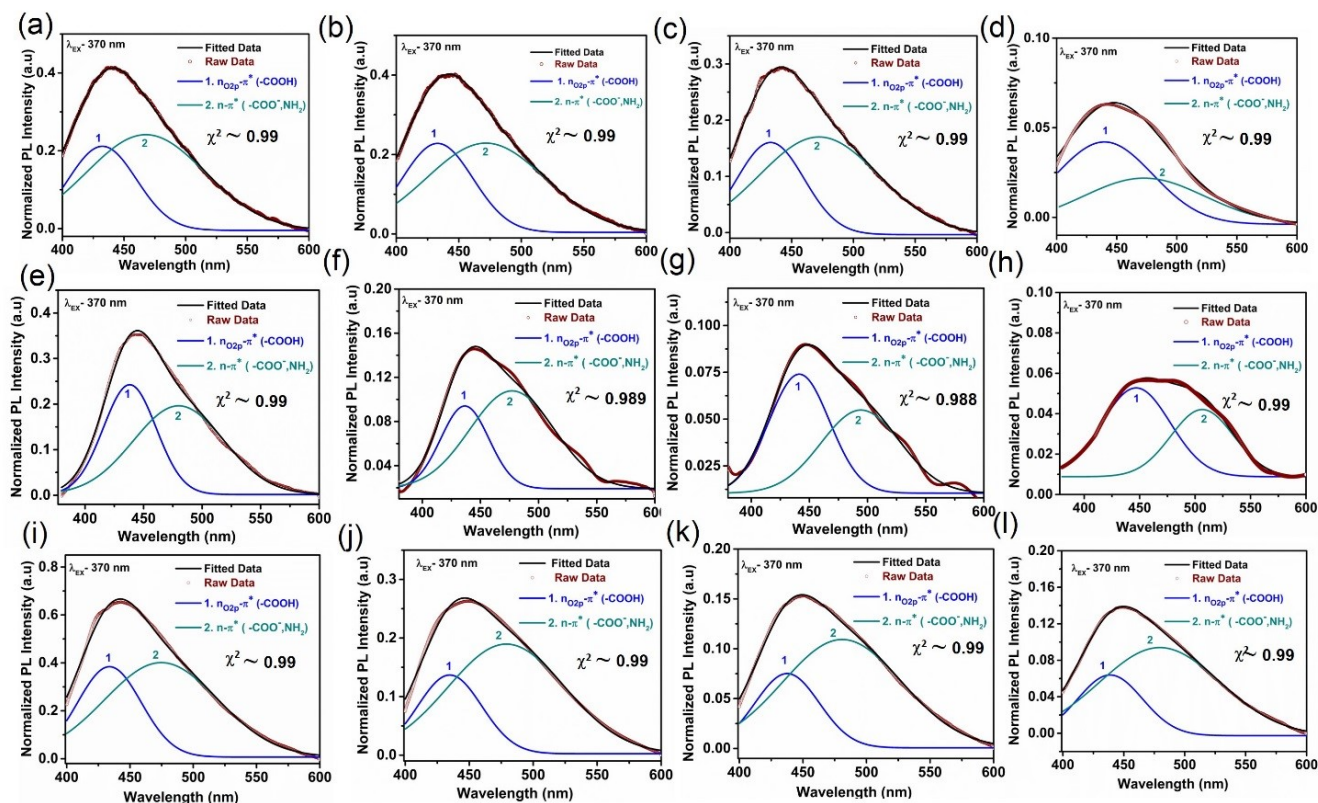
Figure S15: Deconvoluted PL profile of 3A,3B and 3C with (a,e,i) 56 µM (b,f,j) 94 µM (c,g,k) 376 µM and (d,h,l) 658 µM Hg^{2+} respectively at excitation wavelength 370 nm.
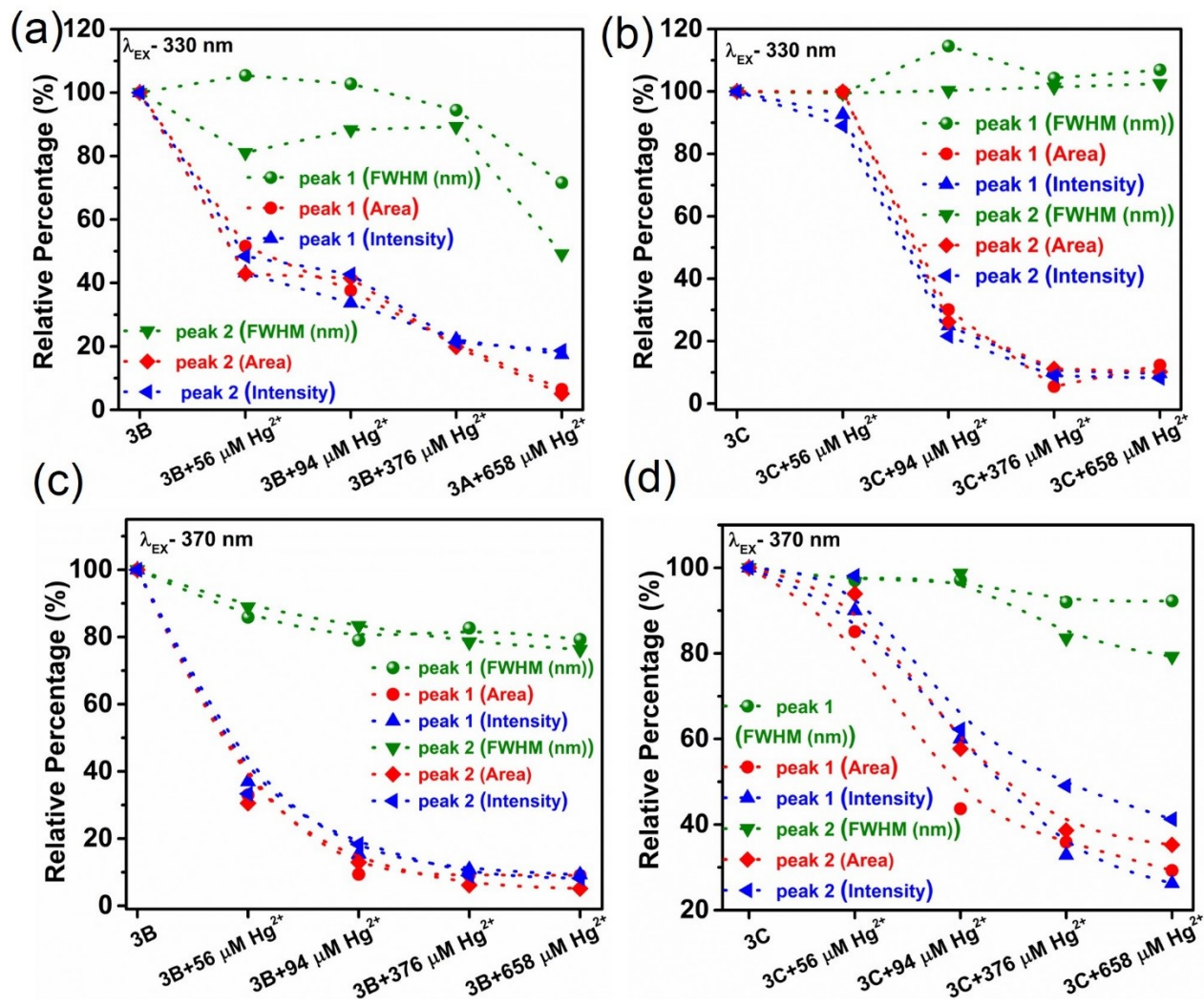
Figure S16: Relative percentage of PL fwhm (nm), area and intensity of (a) peak 1 (π-π^*) and peak 2 (n-π^*) (b) peak 1 (n_{O2P}-π^* -COOH) and (d) peak 2 (n_{O2P}-π^* -COO$^-$, NH$_2$) of 3B and 3C with different Hg^{2+} concentrations.

Section S7: Effect of pH on PL profile after sensing (2.82 mM Hg^{2+}):

Generally, CQD is very sensitive to the medium's pH, depending on the chemical environment and surface functional groups. As the surface functional groups are involved in quenching mechanisms, the PL profile after sensing at different pH is carried out. Our study reveals a decrease in PL emission maxima (λ_{max}) at different pH after Hg^{2+} addition. At pH~7, the emission intensity has almost diminished at 2.82 mM of Hg^{2+} under 330 nm and 370-390 nm excitation wavelength for 3A (Figure. S17a,d). Compared with 3A, the λ_{max} for 3B and 3C becomes significant at 330 nm excitation at three different pHs (Figure S17b,c).

Interestingly, the prominent PL intensity has been noticed at lower (pH~1) and higher (pH~12) pH for all N-CQDs after sensing. At higher pH-12, carboxylate ion (COO-) formation undergoes pπ-pπ conjugation with aromatic ring tends to shrink the electron density at the excited state.[7] These types of conjugation undergo blue shift of the PLE spectra in comparison with pH-7 (Figure S6f). Since the quenching mechanism is strongly associated with static and dynamic processes and less active sites at the excited state, the quenching efficiency is not prominent at pH-12 for all N-CQDs. Interestingly, another possibility of binding between Hg^{2+} with OH$^-$ ion to generate mercury hydroxide production shrinks the accessibility of Hg2+ in the N-CQD surface, enhancing the PL profile at various excitation wavelengths. In contrast, the atomic percentage of carboxylate ion (COO$^-$) and amine contain functional groups that are lower for 3C than the rest of N-CQDs discussed in XPS and zeta potential analyses. The lower percentage results in insufficient active sites for Hg2+ binding and quenching phenomena observed for 3C to be much lower than other 3B and 3A systems.

18
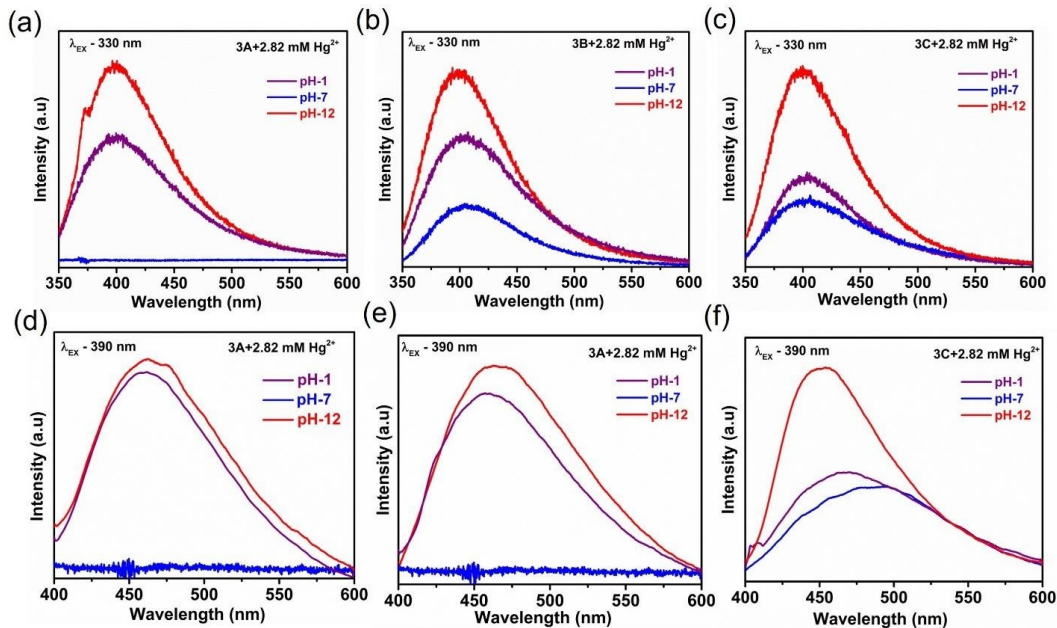
Figure S17: PL maxima of (a,d) 3A (b,e) 3B and (c,f) 3C after addition of 2.82 mM Hg^{2+} at different pH under 330 nm and 370 nm excitation.

Section S8: Functional groups analyses from FTIR Spectra after 2.82 mM Hg^{2+}:

Post FTIR measurement has been carried out of all N-CQDs after 2.82 mM Hg^{2+} to study and correlate with XPS spectra for the activity of the functional groups towards sensing mechanism (Figure S18c). The broad peak around ~3400 cm^{-1} is significantly shrinking due to the unavailability of NH$_2$ groups participating in sensing mechanisms. The O-H stretching frequency remains at ~3200 cm^{-1}, suggesting that Hg^{2+} does not effectively bind with O-H functional groups. The peak is positioned at 1746 cm^{-1}, 1650 cm^{-1}, 1530 cm^{-1}, 1403 cm^{-1}, 1308 cm^{-1}, and 1035 cm^{-1}, originating from C=O, C=C, N-H bending, O-C-O, C-N, and C-O bond, respectively. A noticeable shift of N-H bending mode has been determined due to binding with Hg^{2+}. Moreover, the ~17 cm^{-1} shift of O-C-O (COOH) group clearly explains the interaction with Hg^{2+} and validates XPS and zeta potential analyses.[10]
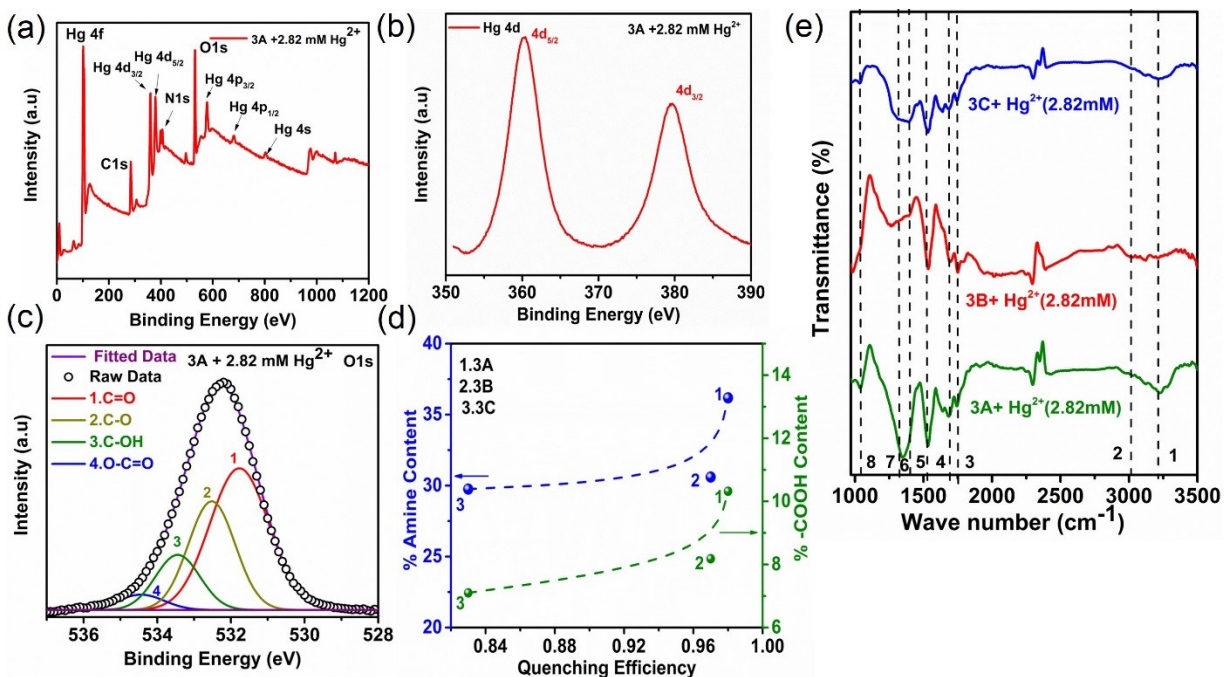
Figure S18: XPS survey spectra of (a) 3A with 2.82 mM Hg^{2+}. High resolution XPS (b) Hg 4d and (c) O1s spectra with 2.82 mM Hg^{2+}(d) Relationship between quenching efficiency of N-CQD (3A,3B, and 3C) towards Hg^{2+} with atomic percentage of amine and COOH functional groups at 370 nm excitation. (e) FTIR spectra of 3A, 3B, and 3C with 2.82 mM Hg^{2+}. (Here, 1-8 denotes different functional groups 1)- O-H stretching, 2) C-H stretching, 3) C=O, 4) C=C, 5) C-N, 6) N-H bending, 7) O- C=O, 8) C-O stretching frequency.

Section S9. UV-Vis Absorbance and Band Gap analyses after quenching:

The UV-Vis absorption and band gap are determined in all N-CQDs in the presence of 2.82 mM Hg^{2+} shown in Figure S19. At 2.82 mM concentration of Hg^{2+}, the n-π* transition at ~322 nm has completely diminished (Figure S19a). In contrast, a broad peak around ~298 nm has been observed, which is the characteristic UV- Vis absorption of Hg $(NO3)_2$. To explain that, UV-Vis absorption of bare $Hg(NO3)_2$ is carried out, showing a broad maximum at ~301 nm (Figure S18a). Thus, quenching effect on absorbance will also influence the change in band gap of N-CQD significantly. The band gap at 3.34 eV is completely diminished at 2.82 mM Hg^{2+} of 3A, concluding its origin due to the defect states. Interestingly, the band gap of $Hg(NO3)_2$ lies at ~3.85 eV, which is almost similar to ~3.8 -4 eV of 3B and 3C (Figure S19b-e).
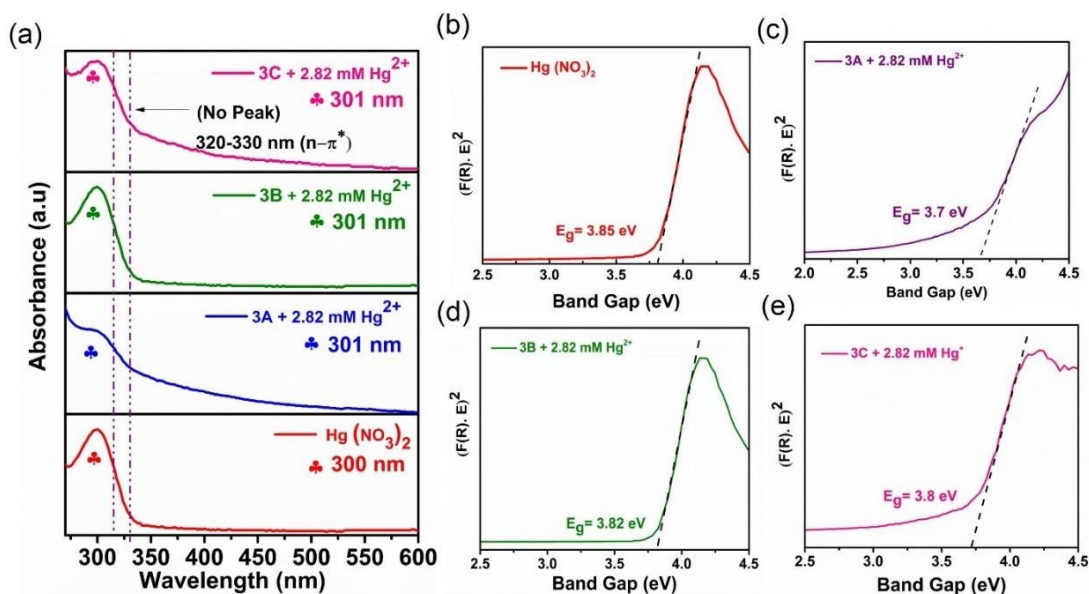
Figure S19: UV-Vis absorption spectroscopy of N-CQD (3A,3B,3C) in presence of Hg^{2+} (conc.2.82 mM). Tauc plot of (b) bare $Hg(NO_3)_2$ (c) 3A (d) 3B and (e) 3C in presence of 2.82 mM Hg^{2+}.
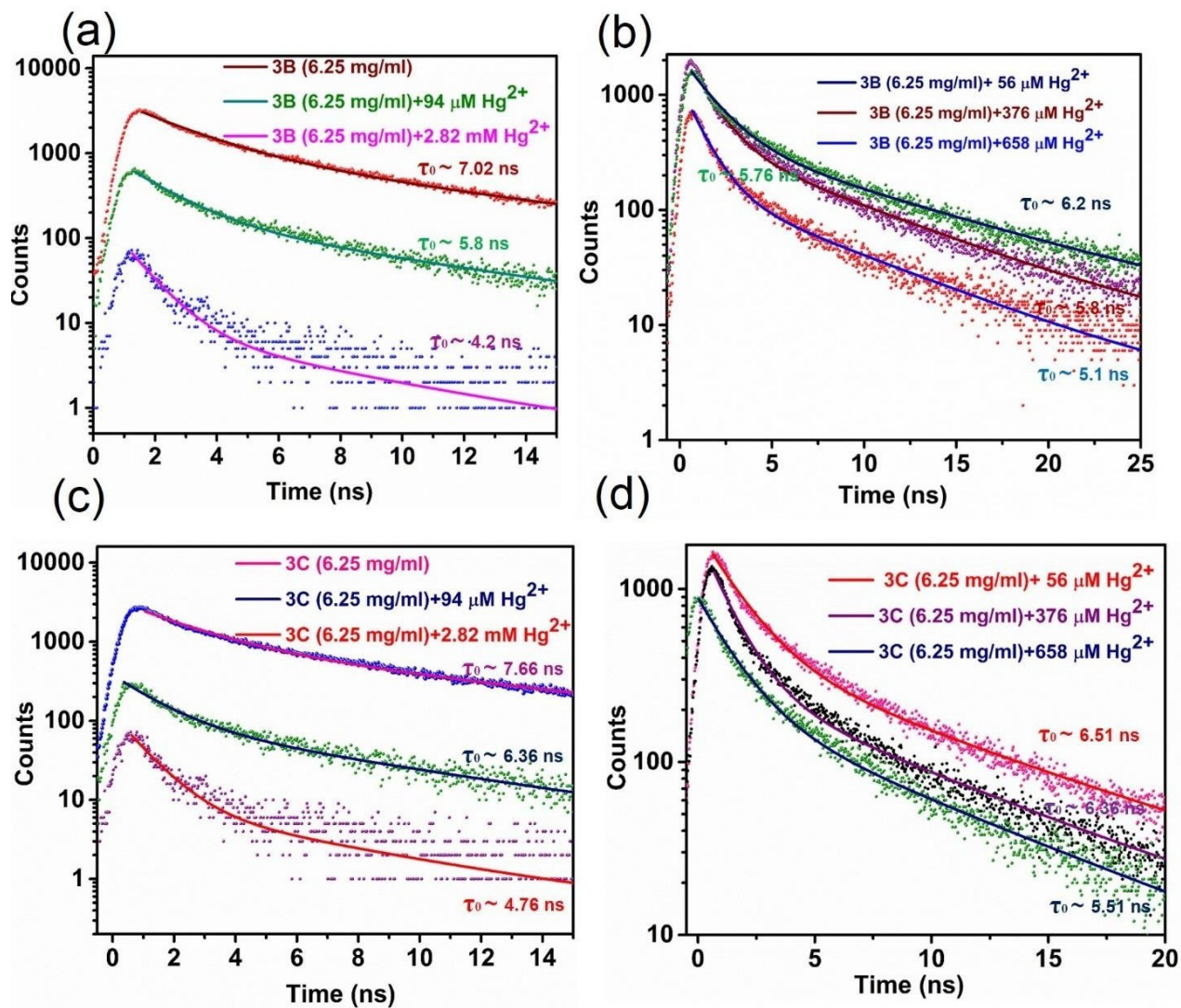
Figure S20: Time-resolved PL decay of (a,b) 3B and (c,d) 3C with 56 μM, 94 μM, 376 μM, 658 μM, 2.82 μM at emission wavelength.
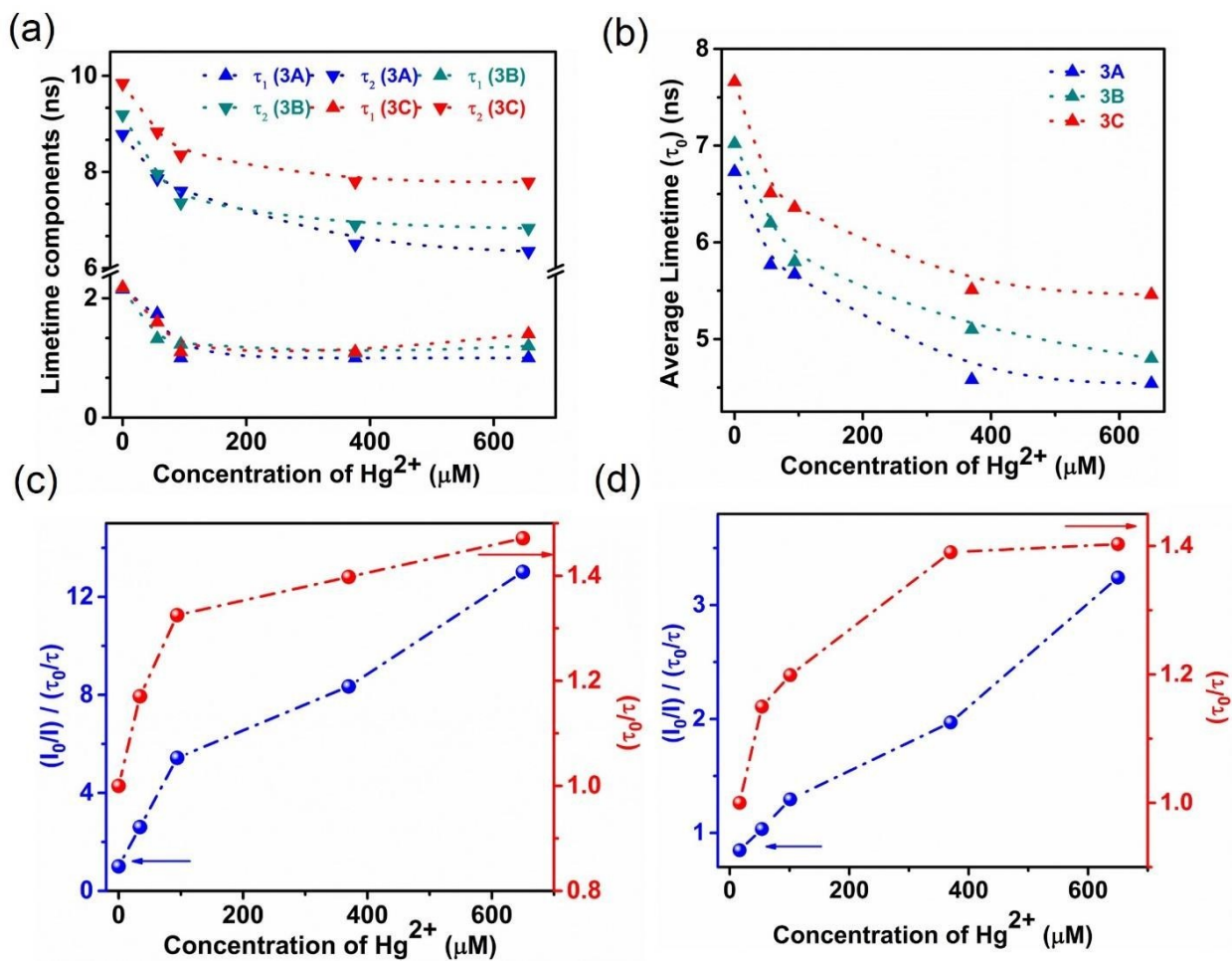
Figure S21: (a) Lifetime components and (b) average lifetime of 3A, 3B, and 3C with concentration of Hg^{2+} from Time-resolved PL decay analyses. (c) Static and dynamic contribution of (c) 3B and (d) 3C with different concentrations of Hg^{2+}.
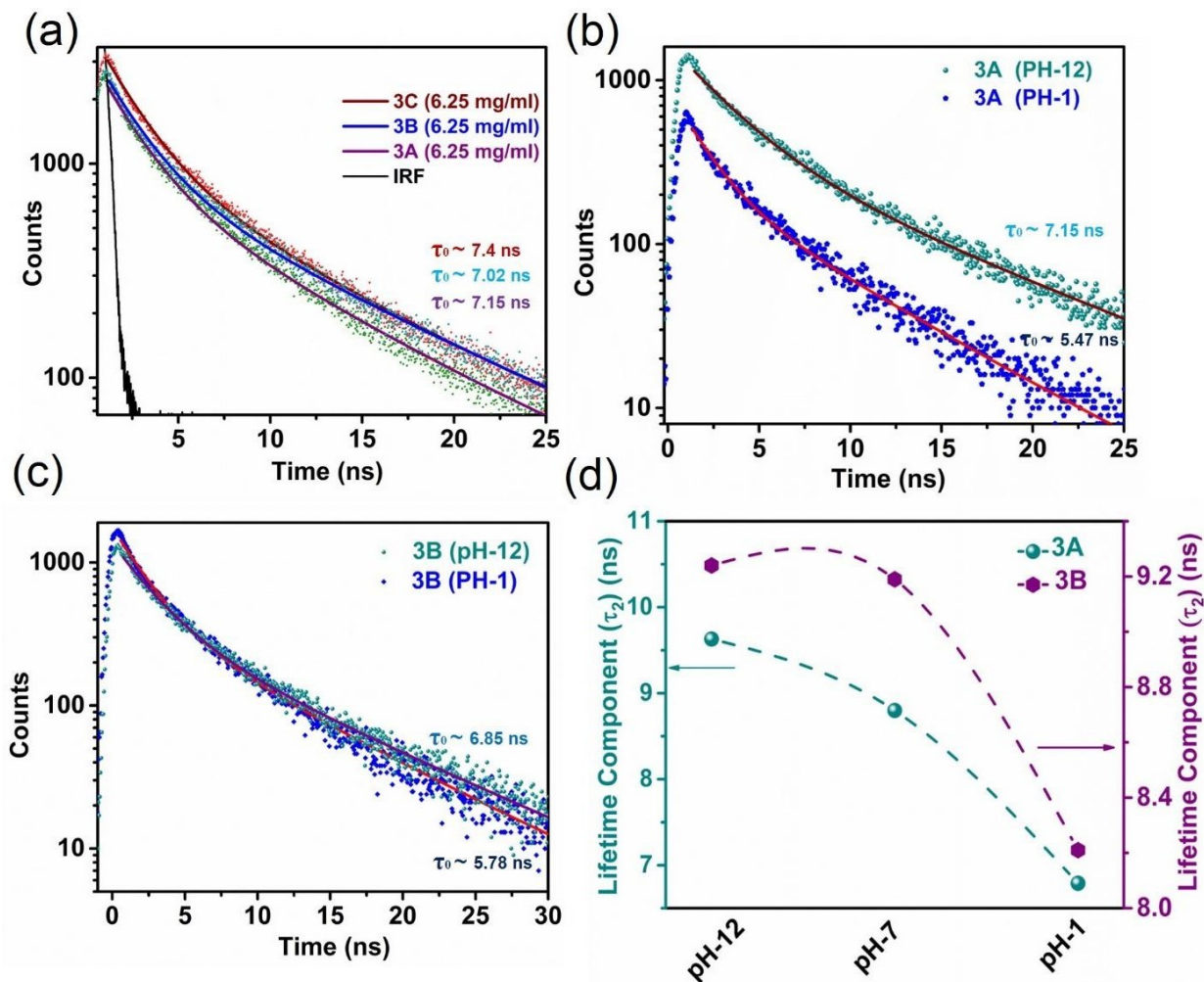
Figure S22: Time-resolved PL decay of (a) N-CQD (3A,3B,3C) at ~506 nm emission wavelength. Time-resolved PL decay of (b) 3B and (c) 3C at pH-1 and pH-12 at emission wavelength. (d) Comparison of PL lifetime component (τ_2) of 3A and 3B at different pH.

The average lifetime increases at higher pH (~12), whereas at lower pH (~1), the lifetime of 3A and 3B decreases (Figure S22). This is because the carboxylate ion (COO-) is relatively stable in the excited state due to electron transfer to the graphitic carbon. However, the protonation of functional groups tends to decrease the stability at the excited states.

Section S10: Analyses of PL signals (Peak area, Intensity) of N-CQD with concentration of Hg^{2+} at 330 nm excitation after EDTA recovery:

The sensitivity of peak1 (π-π^*) and peak 2 (n-π^*) emission towards Hg^{2+} and corresponding PL recovery is carried out at four different Hg^{2+} concentrations (56 µM, 94 µM, 376 µM, and 658 µM). After EDTA addition, the relative percentage of area of peak1 (π-π^*) and peak 2 (n-π^*) are enhanced to 47% (3A), 57% (3A), 14% (3B),15% (3B), 9% (3C), 11% (3C) at 56 µM Hg^{2+}. The result is also consistent with higher Hg^{2+} concentrations (Figure S23). At 376 µM Hg^{2+}, the recovery percentage of peak intensity and area of peak 2 (n-π^*) becomes 37% and 28% (for 3A), 12% and 1.5% (for 3B) and 16% and 2% (for 3C) higher than peak1 (π-π^*). Moreover, the recovery percentage of peak intensity and area of peak 2 (n-π^*) are 1% and 1% (for 3A), 13% and 18% (for 3B) and 8% and 1% (for 3C) higher than peak1 (π-π^*) at 658 µM Hg^{2+}.

Figure S23: Deconvoluted PL profile of 3A,3B and 3C with (a,e,i) 56 µM (b,f,j) 94 µM (c,g,k) 376 µM and (d,h,l) 658 µM Hg^{2+} with 0.034 M EDTA respectively at excitation wavelength 330 nm.

Section S11: Analyses of PL signals (Peak area, Intensity) of N-CQD with concentration of Hg^{2+} at 370 nm excitation after EDTA recovery:

Similar to emission profile at 330 nm excitation, the recovery percentage of peak 1 n_{O2p}-π^* (-COOH) and peak 2 n_{O2p}-π^*/ n_{N2p}-π^* (COO$^-$, NH$_2$ or amide) with Hg^{2+} at 370 nm excitation have been discussed in Figure S24. Under 56 μM Hg^{2+} concentration, the recovery percentage of PL intensity of peak 1 n_{O2p}-π^* (-COOH) and peak 2 n_{O2p}-π^*/ n_{N2p}-π^* are 53.25%, 91.14% (3A), 34.22% (3B), 59% (3B) and 62% (3C), 69.7% (3C) respectively. Subsequently, the recovery of peak area of peak 1 n_{O2p}-π^* (-COOH) and peak 2 n_{O2p}-π^*/ n_{N2p}-π^* are 34.69%, 56.2% (3A), 26.22% (3B), 34% (3B) and 61% (3C), 68.7% (3C) respectively. At 94 μM Hg^{2+}, the recovery percentage of peak intensity of peak 1 and peak 2 are 46%, 74% (3A), 57%, 66% (3B) and 31%, 68% (3C) respectively. Under 376 μM and 658 μM Hg^{2+}, the recovery of intensity of peak 1 becomes 50.4% (3A), 68.79% (3B), 22.22% (3C) and 37.77% (3A), 33.5% (3B), 14.89% (3C) respectively.
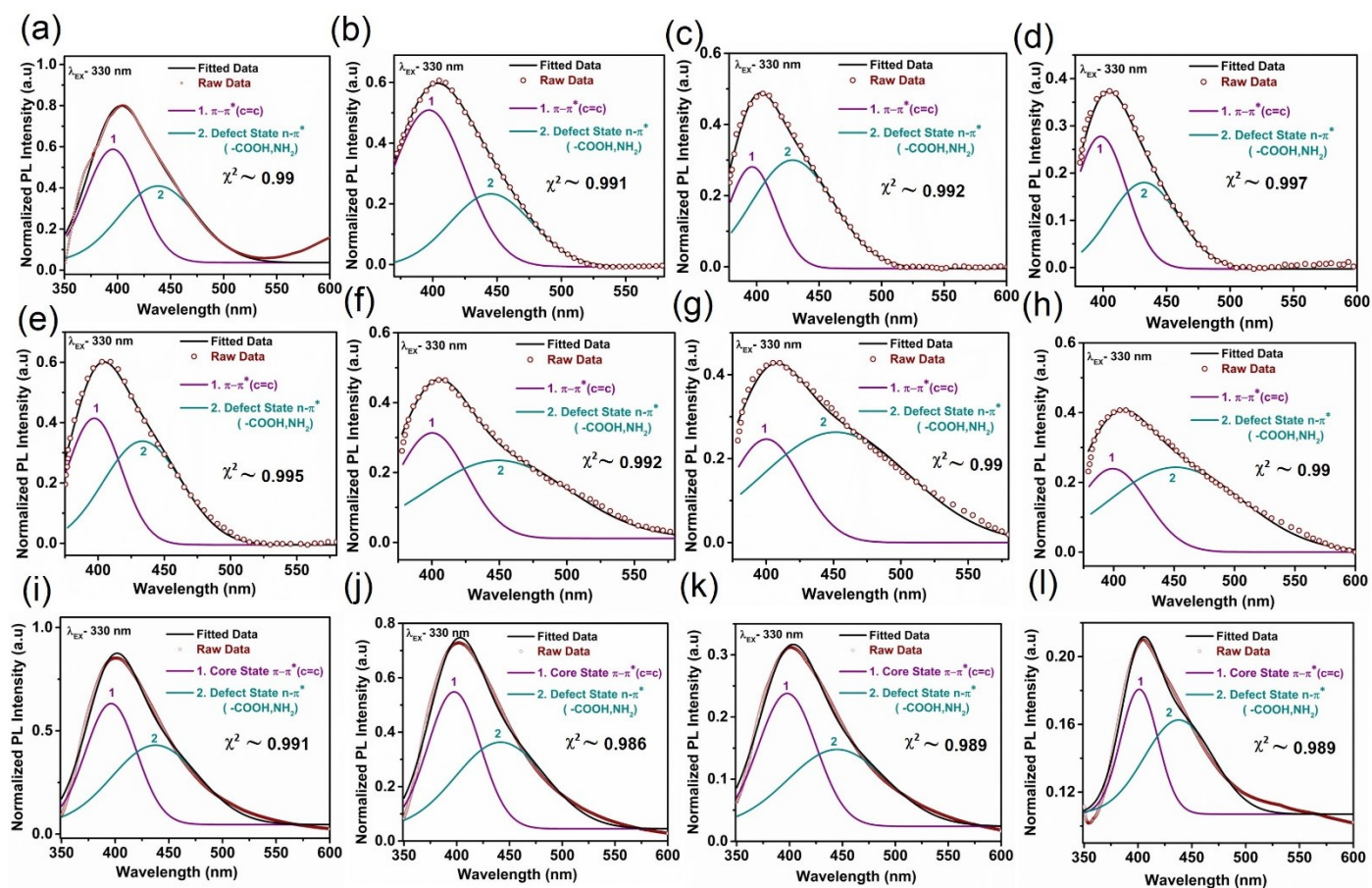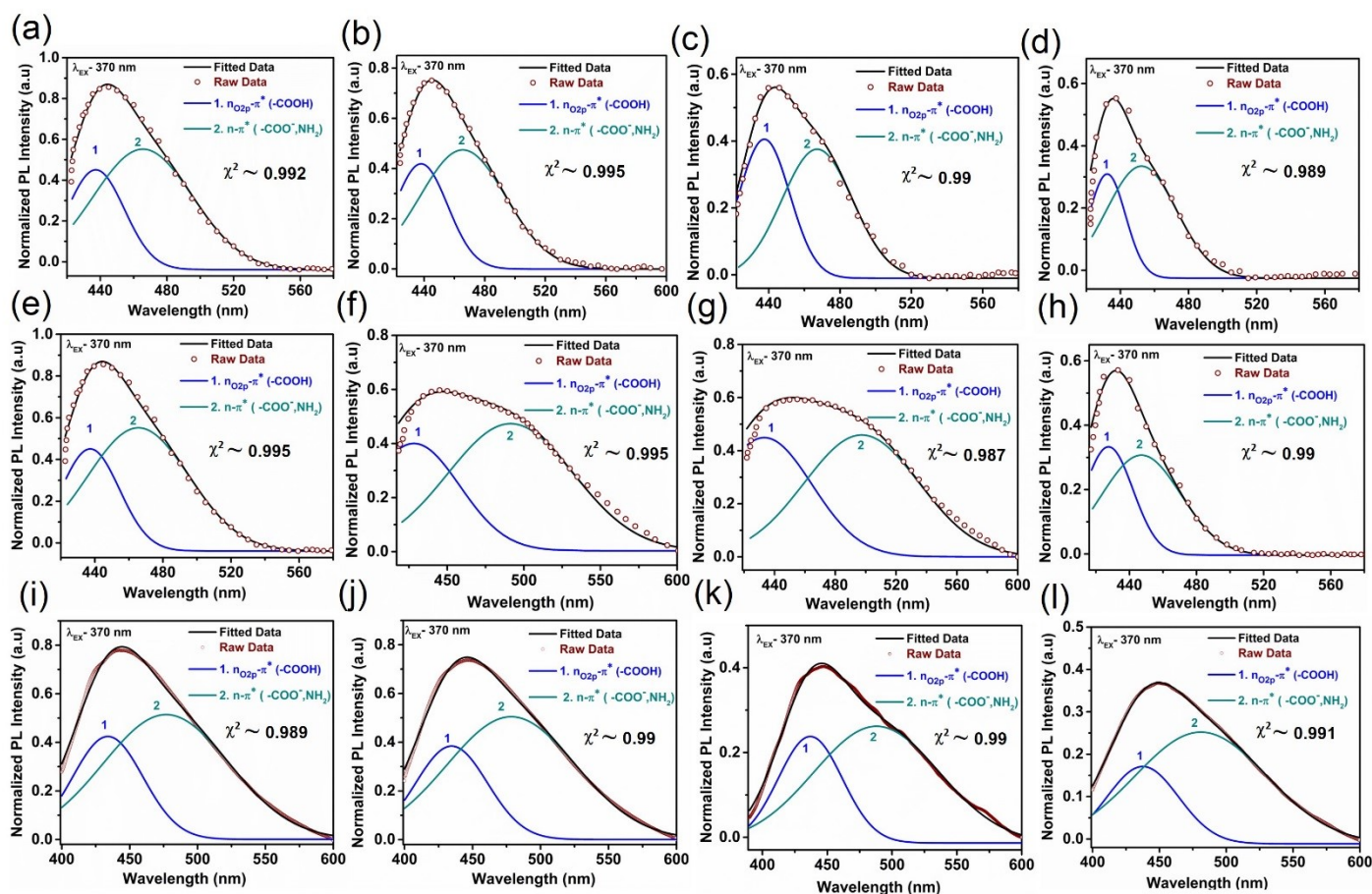

Figure S24: Deconvoluted PL profile of 3A,3B and 3C with (a,e,i) 56 μM (b,f,j) 94 μM (c,g,k) 376 μM and (d,h,l) 658 μM Hg^{2+} with 0.034 M EDTA respectively at excitation wavelength 370 nm.

Section S12: Analyses of PLE profile and PL peak position before and after PL recovery:

The intensity of the PLE profile at ~510 nm emission has been studied with different Hg^{2+} concentrations (56 µM, 94 µM, 376 µM, and 658 µM) before and after EDTA incorporation. The broad peak (PLE maxima) intensity near ~330 nm (core state) remains contracted with increasing the Hg^{2+}. Similarly, the broad shoulder peak between 350-450 nm ($n\text{-}\pi^*$) has also been decreased and associated with the decrement of the core state. The decrement of such intensity illustrates the possibility of ground state (static) quenching. Interestingly, at lower concentrations of Hg^{2+} (56 µM and 94 µM), complete restoration occurs between 350-450 nm excitation, where the relative intensity near ~330 nm becomes 90% and 87%, respectively (Figure. S25a,b). Thus, the result suggests that the efficiency of PLE restoration for defect states predominates over core states. The lesser possibility of PLE restoring core state at 330 nm reduces the percentage of restoration of PL signals of emission peak 1 $\pi\text{-}\pi^*$ (λ_{max} ~390 nm) of N-CQD. At higher concentrations (376 µM and 658 µM) of Hg^{2+}, the percentage of PLE restoration decreases due to the excess amount of Hg^{2+} at the surface of N-CQD (Figure. S25 c,d).
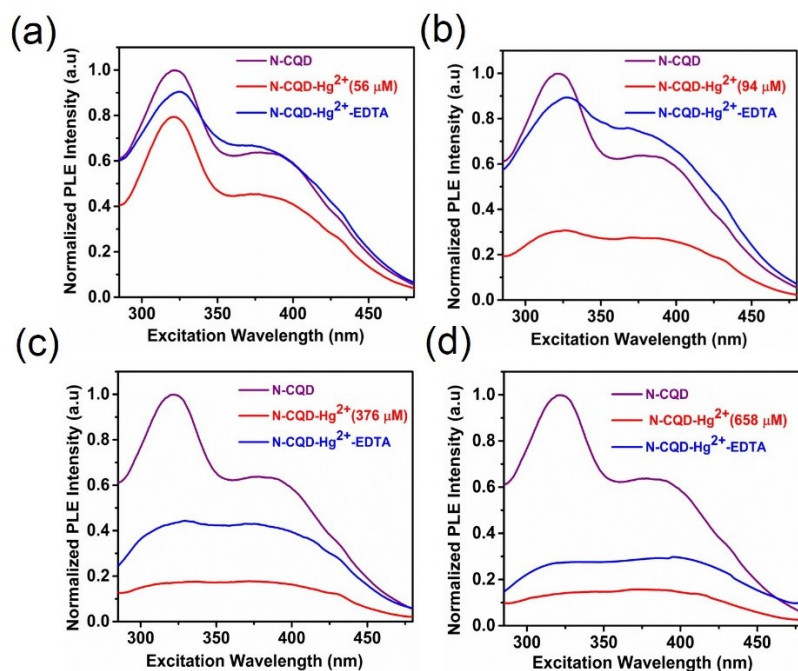
Figure S25: PLE profile of N-CQD (3A) with (a) 94 µM Hg^{2+} (d) 94 µM Hg^{2+}+0.034 M EDTA (b) 376 µM Hg^{2+} (e) 376 µM Hg^{2+}+0.034 M EDTA (c) 658 µM Hg^{2+} and (f) 658 µM Hg^{2+}+0.034 M EDTA at emission wavelength ~510 nm.

Section S13: Analyses of PL intensities of N-CQD (3A) with concentration of Hg^{2+} at 430 nm excitation before and after EDTA:

At 430 nm excitation, the emission profile has been studied with Hg^{2+} concentrations (56 µM, 94 µM, 376 µM, and 658 µM) shown in Figure. S26. The relative intensity of emission maxima (λ_{max}) of 3B decreases to ~40%, ~38%, ~32% and ~28% after 56 µM, 94 µM, 376 µM, and 658 µM Hg^{2+} addition respectively. The PL intensity (λ_{max}) tends to increase after EDTA addition to a value of 92%, 90%, 79% and 56% respectively under the aforementioned Hg^{2+} concentrations respectively.
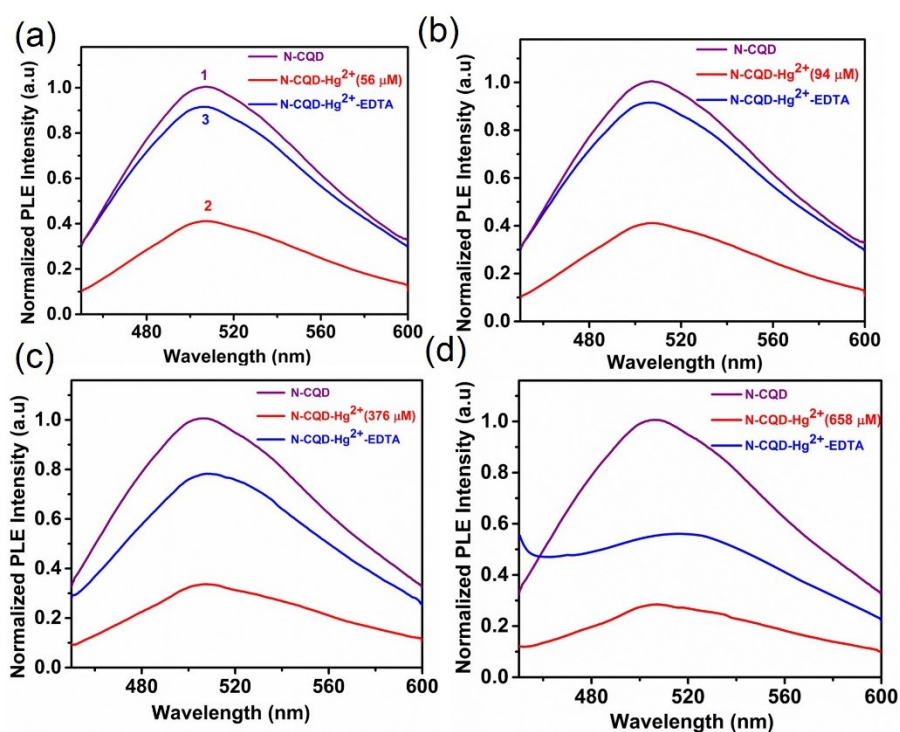

Figure S26: Deconvoluted PL profile of N-CQD (3A) with (a) 94 µM Hg^{2+} and 94 µM Hg^{2+}+0.034 M EDTA (b) 376 µM Hg^{2+} and 376 µM Hg^{2+}+0.034 M EDTA (c) 658 µM Hg^{2+} and 658 µM Hg^{2+} +0.034 M EDTA at excitation wavelength 430 nm.
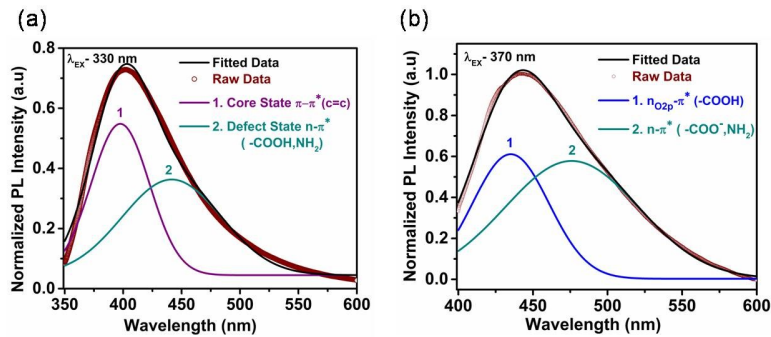
Figure S27: Deconvoluted PL profile of 3A with 94 µM Hg^{2+} and 0.102 M EDTA at excitation wavelength (a) 330 nm (b) 370 nm.
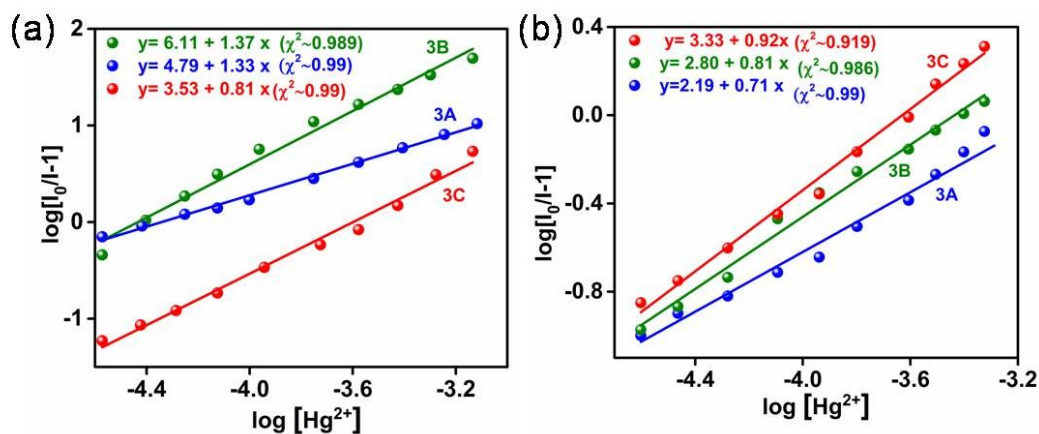
Figure S28: Plot of log $[I_0/I-1]$ vs. log $[Hg^{2+}]$ for the determination of binding constant and binding site for N-CQD (a) before (b) after PL recovery with EDTA.
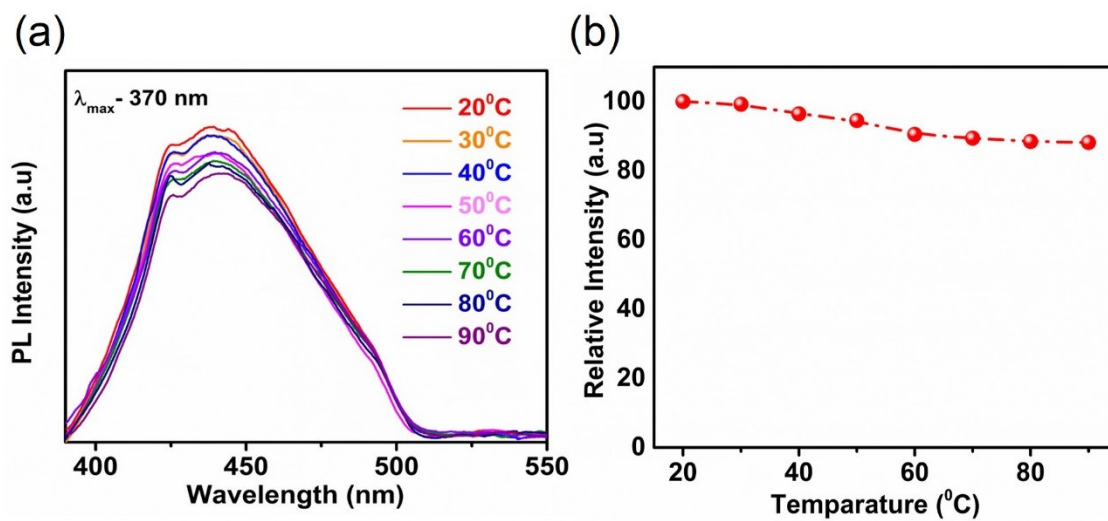
Figure S29: (a,b) Temperature stability of 3A at different temperatures under 370 nm excitation.

The thermal stability of 3A has been determined by measuring PL at different temperatures (20° C to 90°C) (Figure S26). The relative intensity of PL emission decreases linearly to 40^0 C and tends to reduce to 88.4% at 90° C (Figure S24f). The retention of PL intensity of N-CQD with temperature.

Table S1: Preparation of N-CQD and different concentration of Hg^{2+} for PL measurement.

SL No	Sample Stock (ml)	Hg^{2+} stock (ml)	DI (ml)	Hg^{2+} conc. (M)
1	0.1	0	3	0
2	0.1	0.02	2.98	1.8×10^{-5}
3	0.1	0.04	2.96	3.7×10^{-5}
4	0.1	0.06	2.94	5.6×10^{-5}
5	0.1	0.08	2.92	7.5×10^{-5}
6	0.1	0.1	2.90	9.4×10^{-5}
7	0.1	0.2	2.80	1.88×10^{-4}
8	0.1	0.3	2.70	2.82×10^{-4}
9	0.1	0.4	2.60	3.76×10^{-4}
10	0.1	0.5	2.50	4.7×10^{-4}
11	0.1	0.7	2.30	6.58×10^{-4}
12	0.1	3	0	0.00282

Table S2: Adsorption energy (eV) of Hg on different active sites (pyridinic, amine, carboxylic group) of N-CQD.

COOH-Hg	NH$_2$-Hg	Pyridinic N-Hg	COOH-Cd	NH$_2$-Cd	Pyridinic N-Cd	COOH-Pb	NH$_2$-Pb	Pyridinic N-Pb
0.029 eV	0.093 eV	0.102 eV	1.06 eV	1.14 eV	1.15 eV	2.72 eV	2.85 eV	3.1 eV

*CD: Carbon Dot; #N-CQD: Nitrogen doped Carbon Quantum dot; †FCDs: Fluorescent carbon dots, $ TFIC MNPs: TSRh6G-b-CD/Fe₃O₄@ SiO₂-nanoparticle, GQD: Graphene quantum dots.

Table S3: Comparison of sensing Performance of N-CQD.

Sensing probes	Main Application	Medium	Detection Limit	Signal	Q.Y	Ref
CD	Hg^{2+}	Ultrapore Water	0.23 µM (Range-0-25 µM)	PL	15.7	11
CD	Hg^{2+}	Phosphate buffer	$2.69*10^3$ nmol/ L (Range- 10^{-7}– 2.69×10^{-6} M)	PL	-	12
N-CQD	Hg^{2+}	Phosphate buffer	$2.3*10^2$ nmol/L (Range- 10^{-7}– 2.69×10^{-6} M)	PL	-	13
N/C-dots	Hg^{2+}	Ultrapore Water	2 µM (Range-0-40µM)	PL	25.2	14
Graphitized CD	Hg^{2+}	Deionized water	35 nmol/ L (Range- 0-10⁻⁶ mol/L)	PL	25	15
FCDs	Hg^{2+}	Deionized water	20 (Range- 0.1– 1.2 µmol L^{-1})	PL	36	16
CD	Hg^{2+} and Cys	ultrapure water	0.017 µM (Range- 2 to 22 µM)	PL	15.3	17
TFIC MNPs	Hg^{2+}	ultrapure water	$5.04*10^{-6}$ mol/L (Range- 4.0×10^{-6} to 16×10^{-6} mol/L)	PL	-	18
CQDs-Tb3+	Hg^{2+}	Water	38.1 nM (Range-1-6µM)	PL	-	19
CD	Hg^{2+}	Water	9 nM (Range-0-40µM)	PL	-	20
GQD	Hg^{2+}	ultrapure water	0.12 µM (Range-0.15-20 µM)	PL	15.1	21
N-CQD	Hg^{2+}	Deionized water	0.209 µM (Range-0-100 µM)	PL	54	This Work

References:

1. D. Roy, S. Sarkar, K. Bhattacharjee, K. Panigrahi, B.K. Das, K. Sardar, S. Sarkar, K.K. Chattopadhyay, *Carbon*., 2020, **166**, 361-373.

2. J. Schneider, C.J. Reckmeier, Y. Xiong, M.von Seckendorff, A.S. Susha, P. Kasák, A.L. Rogach, *J. Phys. Chem. C*., 2017, **121**, 2014-2022.

3. X. Luo, P. Bai, X. Wang, G. Zhao, J. Feng, H. Ren, *New J Chem*., 2019, **43**, 5488-5494.

4. J. Tan, R. Zou, J. Zhang, W. Li, L. Zhang, D. Yue, *Nanoscale*., 2016, **8,** 4742-4747.

5. S. Muthulingam, K.B. Bae, R. Khan, I.H. Lee, P. Uthirakumar, *RSC Adv.,* 2015, **5**, 46247-46251.

6. Y. Han, H. Huang, H. Zhang, Y. Liu, X. Han, R. Liu, H. Li, Z. Kang, *ACS Catal.*, 2014, **4** , 781–787.

7. S. Lai, Y. Jin, L. Shi, R. Zhou, Y. Zhou, D. An, *Nanoscale*., 2020, **12**, 591-601.

8. C.B. Ma, Z.T. Zhu, H.W. Wang, X. Huang, X. Zhang, X. Qi, H.L. Zhang, Y. Zhu, X. Deng, Y. Peng,Y. Han, *Nanoscale*., 2015, **7**, 10162−10169.

9. Y. Zhan, T. Geng, Y. Liu, C. Hu, X. Zhang, B. Lei, J. Zhuang, X. Wu, D. Huang, G. Xiao, B. Zou, *ACS Appl. Mater. Interfaces.,* 2018, **10**, 27920-27927.

10. M.C. Terkhi, F. Taleb, P. Gossart, A. Semmoud, A.Addou, *Chemistry*., 2008, **198(2-3)**, 205-214.

11. .R.Zhang, W. Chen, *Biosens. Bioelectron*., 2014, **55**, 83-90.

12. H.M.Gonçalves, A.J. Duarte, J.C.E. da Silva, *Biosens. Bioelectron.,* 2010, **26**, 1302-1306.

13. H. Gonçalves, P.A. Jorge, J.R.A. Fernandes, J.C.E. da Silva, *Sens. Actuators.B*., 2010, **145**, 702-707.

14. L. Li, B. Yu, T. You, *Biosens. Bioelectron.*, 2015, **74**, 263-269.

15. Y. Liu, C.Y. Liu, Z.Y. Zhang, *Appl. Surf. Sci.,* 2012, **263**, 481-485.

16. Z.H. Gao, Z.Z. Lin, X.M. Chen, Z.Z. Lai, Z.Y. Huang, *Sens. Actuators, B*., 2016, **222**, 965-971.

17. F. Yan, D. Shi, T. Zheng, K. Yun, X. Zhou, L. Chen, *Sens. Actuators, B*., 2016, **224**, 926-935.

18. W. Wang, Y. Zhang, Q. Yang, M. Sun, X. Fei, Y. Song, Y. Zhang and Y. Li, *Nanoscale* 2013, **5(11)**, 4958-4965.

19. H. Wu and C. Tong *Anal. Chem.* 2020, **92(13)***,* 8859-8866.

20. J. Zhao, M. Huang, L. Zhang, M. Zou, D. Chen, Y. Huang and S. Zhao, *Anal. Chem.* 2017, **89(15)**, 8044-8049.

21. L. Li, G. Wu, T. Hong, Z. Yin, D. Sun and F.S. Abdel-Halim and J.J. Zhu, *ACS Appl. Mater. Interfaces* 2014, **6(4)**, 2858-2864.